GENERATION OF HIGH CONCENTRATION NANOPARTICLES FOR FILTRATION STUDIES

Da-Ren Chen and David Y. H. Pui

Particle Technology Laboratory
Mechanical Engineering Department
University of Minnesota
Minneapolis, MN 55455, U.S.A.

ABSTRACT

Nanoparticle filtration is important in the recovery of nanoparticle products from materials synthesis processes, and for preventing nanoparticle emissions in the environment and protecting workers against exposure to nanoparticles. Theories have shown that the penetration of nanoparticles through the filter would increase due to thermal rebound between the nanoparticles and filter collection surfaces. In this study, we report on preliminary results of an experimental study of nanoparticle penetration through a model filter. In addition, a high concentration nanoparticle generator has been developed with high mass-throughput. It will be used to challenge high efficiency filters so as to obtain the penetration values. Additional beneficial effects will include the production of industrial quantity of nanoparticles for pharmaceutical and materials applications.

INTRODUCTION

Nanostructured particles and materials, and the physical or chemical combination of substances at the nanometer scale, can result in the discovery of new innovative materials for rechargeable batteries, ceramic fuel cells and solar cells, which can lead to the advancement of clean energy conversion and storage systems. Traditionally, the synthesis route for producing nanoparticles is based on the solution processing technique derived from established solution chemistry. The technique is restricted to limited combinations of constituents for the synthesis process. Gas-phase processing is increasingly used because of its versatility and its

applicability to most materials. One of the challenges in gas-phase processing is to collect nanoparticle products from reactors efficiently. Filtration is one of the principal methods for collecting the nanostructured materials. Further, it is important for preventing nanoparticle emissions in the environment and for protecting workers against exposure to nanoparticles.

It is well known that the filtration efficiency vs. particle size curve has a characteristic v-shape with its minimum between 0.1 and 0.3 μm. Figure 1 shows that the efficiency increases with increasing particle size due to inertial impaction and interception mechanisms, and also increases with decreasing particle size due to diffusion mechanism. The minimum occurs during the transition from the impaction/interception to diffusion mechanisms. While theories for particles larger than 50 nm is well developed, there is insufficient understanding of the filtration mechanism in the nanometer particle size range, i.e., 1 nm < Dp < 50 nm. From classical filtration theories, the collection efficiency should approach 100% for nanoparticles due to the diffusion mechanism. However, it is also commonly known that gas molecules can penetrate through fibrous and membrane filters due to thermal rebound between the molecules and filter surfaces. Consequently, the filtration efficiency should begin to fall off when particles approach molecular dimensions, i.e., nanometer sizes. There are recently some limited theoretical (Wang and Kasper, 1991) and experimental evidences (Ichitsubo et al., 1996) to suggest that nanoparticles would penetrate through the filter media due to thermal rebound effects.

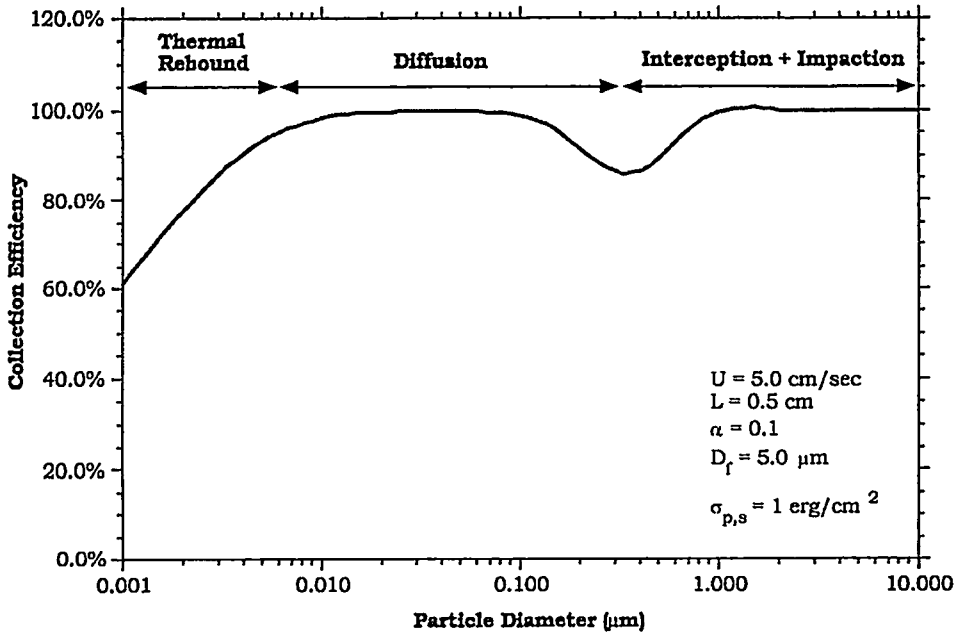

Figure 1. A theoretical filter efficiency curve showing a local minimum at 0.3 μm and the rapid decrease in efficiency (increased penetration) below 10 nm.

Nanoparticles are producing in increasing quantity in materials industry because materials in the nanostructure form possess many desirable properties, including hardness improvement, internal friction reduction (i.e., improved ductility), melting point reduction, and special optical and magnetic properties (e.g., Kofman et al, 1994; Endo et al, 1996; Lin et al, 1995). These properties are the basis of many so-called 'high-tech' applications, including quantum dots, drill bit coatings, fuel cells, solar cells, and tunable laser, and so they promise to revolutionize the materials industry. Production of such materials via the aerosol route provides enhanced levels of materials purity and production control. Penetration of nanoparticles through the filter media would reduce the quantity of recovered nanoparticle products, and would allow nanoparticle emissions in the environment. Nanoparticles are also by-products of many high-tech coating processes (Chan et al., 1995) for thermal or corrosion resistance or for increasing the surface hardness, and in emissions from semiconductor processing equipment and combustion engines. As a result, workers in many modern manufacturing facilities have increasing potential for exposing to nanoparticles emissions.

There is an increased awareness in the occupational health community on the possible adverse health effects of exposure to nanometer particles (e.g., Cheng et al., 1993, 1996; Ferin, 1994; Donaldson et al, 1996; Oberdörster et al., 1992, 1995; Ferin et al., 1990). It has been speculated that nanometer particles depositing in the human respiratory tract may enter the interstitial spaces and may penetrate through the cell membrane, so that even relatively insoluble material may pass beyond the respiratory tract. Those which are retained in the lung may become sequestered and remain there for very long periods. Recent intratracheal injection studies using rats, reported by Donaldson et al. (1996), have shown that material which is relatively inert for micrometer-sized particles (e.g., titanium dioxide) can be highly inflammogenic for particles in the nanometer size range. It is clearly suggested, therefore, that nanometer particles may, depending on their chemical composition, be associated with the possibility of serious ill-health. Therefore, the present study will allow a detailed understanding of nanoparticle filtration and provide a firm basis for developing a new generation of particle removing devices/systems for protecting workers from nanoparticles exposures, and for collecting nanoparticle products from reactors for high-tech applications.

In this paper, we will report on preliminary results of an experimental study of nanoparticle penetration through a model filter. In addition, a high concentration nanoparticle generator has been developed with high mass throughput. It will be used to challenge high efficiency filters so as to obtain

penetration values. Additional beneficial effects will include the production of industrial quantity of nanoparticles for pharmaceutical and materials applications.

NANOPARTICLE FILTRATION EFFICIENCY

The filtration efficiency of nanoparticles was studied both experimentally and theoretically. A model screen filter was used for the particle penetration study. Nanoparticles in the size range of 3 to 20 nm were generated as test aerosols and the penetration of these particles through the model filter was measured.

Silver nanoparticles were produced using the evaporation-condensation technique. The nanoparticles were then passed through a radioactive neutralizer to obtain a bipolar charge distribution. This was followed by a Nanometer Differential Mobility Analyzer (Chen et al., 1998) that was used to classify the silver aerosol into a monodisperse size fraction. The upstream and downstream concentrations of the screen filter were measured by an ultrafine condensation particle counter (UCPC, Model3025A, TSI. Inc., St. Paul, MN). A tape heater controlled the air temperature inside the chamber. A thermal couple that was installed close by the screen measured the aerosol temperature.

The screen-type filter media were 635-mesh, 270-mesh, and 200-mesh type 304 stainless steel wires screens with openings of 0.0008", 0.0021" and 0.0034", respectively. The aerosol flow rate through the screen holder chamber was kept at 1.5 lpm. To study the electrostatic effect, penetration of neutralized and singly charged particles were measured and compared with Cheng and Yeh's theory.

Figure 2(a) shows the penetration of singly charged particles through the 635-mesh screen. The experiments were performed for particle diameter smaller than 15 nm and with different number of screens (n). As shown in the results, the experimental penetration deviates from Cheng and Yeh's theory for particles smaller than 10 nm. The experimental penetration is lower than that predicted from theory. This is in the opposite direction of thermal rebound effect. The lower penetration has been attributed to the enhanced collection of the charged particles by the metal screen due to electrostatic effect. Figure 2(b) shows the penetration of neutralized particles through three different mesh screens. The experimental penetration values are shown to agree well with Cheng and Yeh's theory.

Measurements were performed at elevated temperature of 50-80°C. Figure 2(c) shows that the results follow closely with the theory of Cheng and Yeh down to 10 nm. Increased penetration is observed for particles smaller than 5 nm and at elevated temperature of 80°C, suggesting the possibility of thermal rebound between the nanoparticles and the screen filter. Additional experiments will be performed with different pairs of particle and screen types.

Figure 2. Experimental penetration of nanoparticles through a model screen filter: (a) singly charged particles through 635 mesh screen, (b) neutralized particles through different mesh screens, (c) neutralized particles through different mesh screens at elevated temperature of 50-80°C.

HIGH CONCENTRATION NANOPARTICLE GENERATOR

A multiple-nozzle arrangement of electrospray has been developed to produce high mass-throughput of nanoparticles. Electrospray has been used to produce nanoparticles from solutions or colloidal suspensions. It is capable of producing particles 10-100 times smaller than the conventional pneumatic atomization technique. This will allow the product materials to have 100-10,000 times larger surface area than those produced from the conventional technique, for a given quantity of spray solution. The increased surface forms the basis of enabling technology for several important applications, e.g., fast response and high bioavailability for drug products.

The electrospraying system setup and the details of the capillary tube are shown in Figure 3 (Chen and Pui, 1997). The spraying chamber is in the point-to-plate configuration with the capillary tube facing the plate. An orifice is located on the center of the plate allowing the produced particles to enter the neutralization chamber. A coaxial tube allows CO_2 to flow as a sheath surrounding the capillary tube for suppressing possible corona discharge. Compressed air is supplied from the top of the chamber in order to transport the particles through orifice. Liquid with the desirable solute materials is fed from a programmable syringe pump.

A negative high voltage is applied to the plate and the neutralization chamber. The capillary tube is connected to an electrometer that is used to measure the spraying current. The current reading gives a measure of the particle concentration. At a sufficiently high voltage, the liquid meniscus from the capillary forms a cone jet shape. Liquid column issuing from the tip of cone jet is of the nanometer dimension. The instability of the liquid column causes it to break up into nanometer size particles. The size of the produced liquid droplets can be further reduced by the evaporating the solvent of a known concentration solution.

One limiting factor in deploying the electrospraying technique is that a single spray-nozzle dispenses only a small quantity of solution in μl/min. A major challenge will be to increase the mass-throughput from the sprayer. We have successful implemented a multiple-nozzle electrospray that will allow 1,000 to 10,000 times higher mass throughput rate than the single-nozzle electrospray

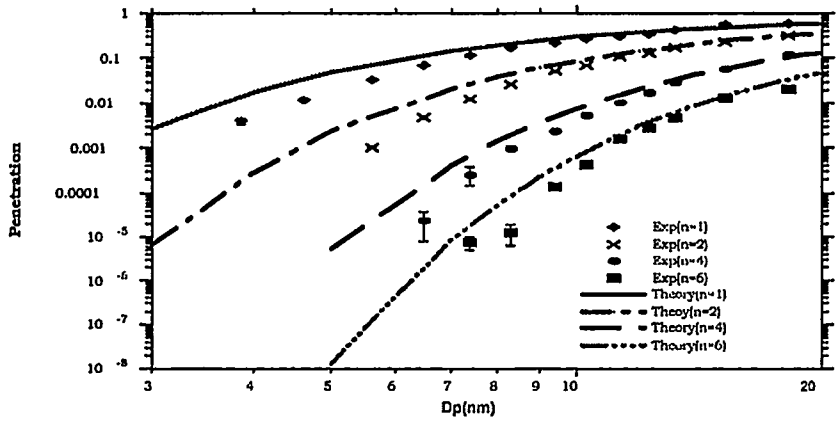
Penetration
Dp(nm)
Exp(n=1)
Exp(n=2)
Exp(n=4)
Exp(n=6)
Theory(n=1)
Theory(n=2)
Theory(n=4)
Theory(n=6)

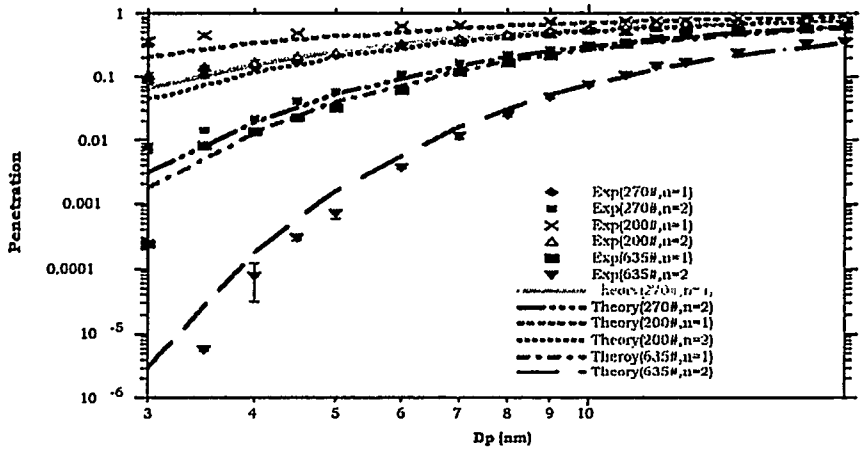
Penetration
Dp (nm)
Exp(270#,n=1)
Exp(270#,n=2)
Exp(200#,n=1)
Exp(200#,n=2)
Exp(635#,n=1)
Exp(635#,n=2
Theory(270#,n=2)
Theory(200#,n=1)
Theory(200#,n=2)
Theroy(635#,n=1)
Theory(635#,n=2)

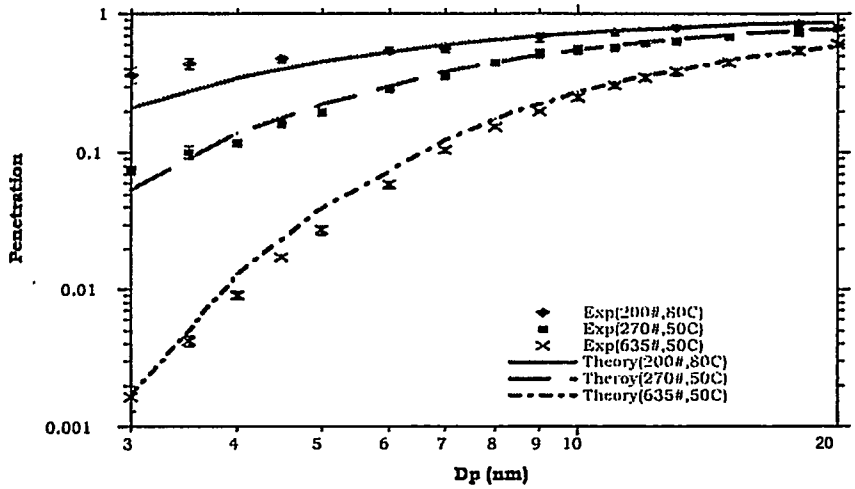
Penetration
Dp (nm)
Exp(200#,80C)
Exp(270#,50C)
Exp(635#,50C)
Theory(200#,80C)
Theroy(270#,50C)
Theory(635#,50C)

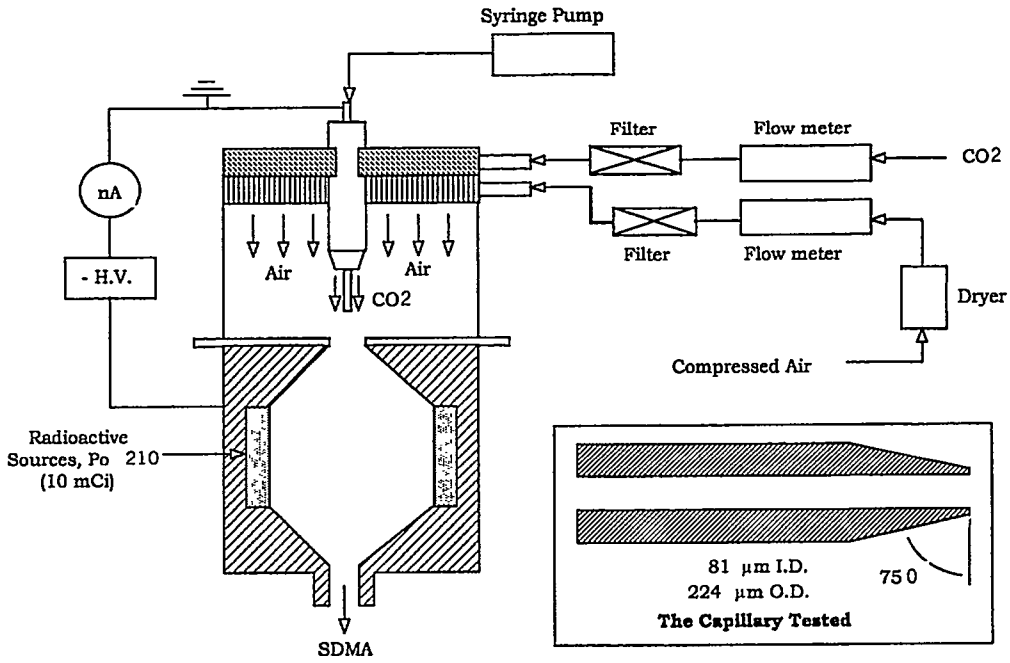

Figure 3. Schematic diagram of a single nozzle electrospray nanoparticle generator.

A single electrospray nozzle can deliver only a limited range of feedrate within the operating envelope of the sprayer. The feedrate can be increased by using multiple nozzles bundled together. The challenge in spraying highly charged nanoparticles from tightly packed bundle of nozzles is to overcome the space charge effect of these nanoparticles. The voltage required to form the cone-jet mode increases with decreasing inter-capillary distance.

Figure 4 shows the voltage required as a function of inter-capillary distance for three nozzle patterns. The voltage required for a single capillary is 7,500 V. As the inter-capillary distance decreases, a higher voltage is required to "expel" the high charged nanoparticles away from the nozzles in order to form the cone-jet mode. Ultimately, the required voltage reaches the breakdown electric field which defines the closest distance for the inter-capillary spacing.

Three different arrangement of the nozzle placement pattern is shown in Figure 5, i.e., the rectangular pattern, the diamond pattern, and the circular pattern. Figure 4 shows that the circular pattern requires the least voltage to form the cone jet mode. It infers that the circular pattern allows the most compact bundle arrangement for the capillaries without breakdown in electric field. With the circular pattern, it is possible to put 1,000 nozzles within a 3" diameter disk that is a typical area to operate a single spray nozzle. It thereby increases the mass

throughput by a factor of 1,000 times. The increase mass throughput will make it attractive for possible industrial applications.

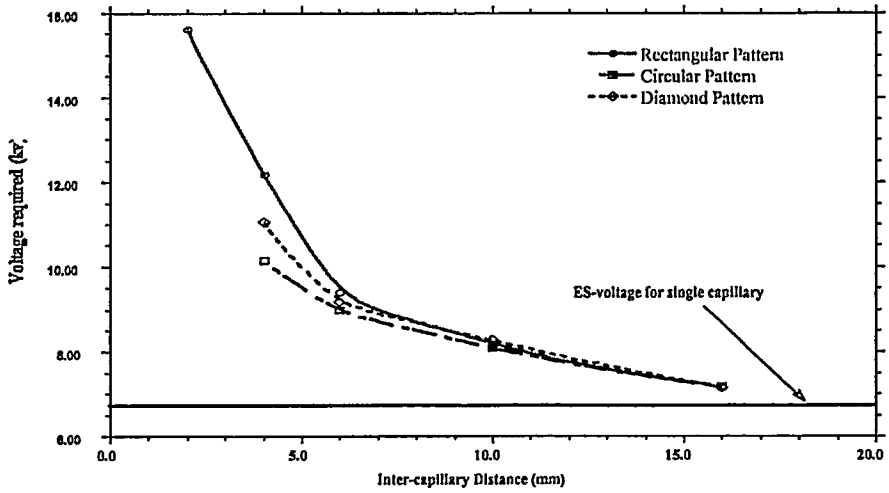

Figure 4. Voltage required to form the cone-jet mode as a function of inter-capillary distance for three nozzle patterns.

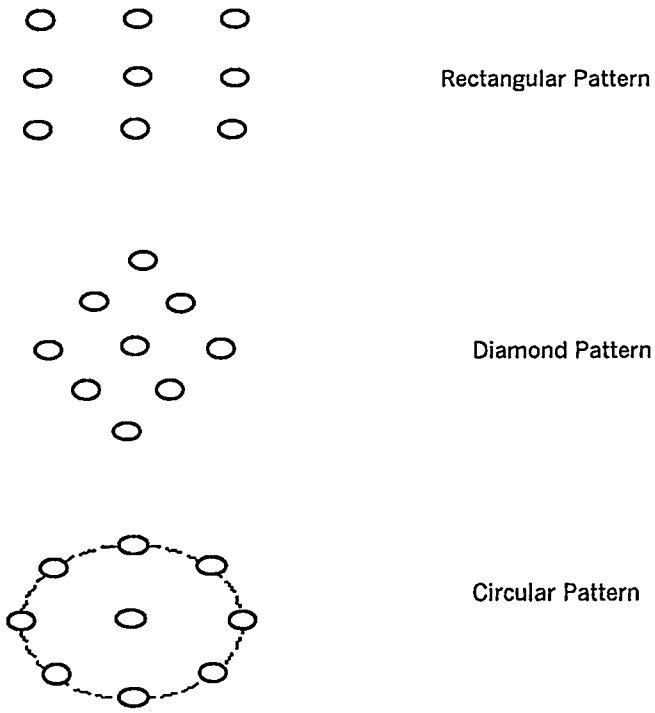

Figure 5. Three arrangements of nozzle placement pattern under investigation.

ACKNOWLEDGEMENT

This work was supported by the U.S. Department of Energy through a grant from the Office of Basic Energy Sciences.

REFERENCES

Chan, T. L., Rouhana, S. W., Mulawa, P. A., and Reuter, R. J., (1995) "Occupational Health Assessment of the High Velocity Oxy-Fuel Thermal Metal Spray Process," *Appl. Occup. Environ. Hyg.*, **10**(5) 482-487.

Chen, D. and D. Y. H. Pui (1997) "Experimental investigation of scaling laws for electrospraying: Dielectric constant effect," *Aerosol Sci. Technol.* **27**, 367-380.

Chen, D., D. Y. H. Pui, D. Hummes, H. Fissan, F. R. Quant and G. J. Sem (1998) "Design and Evaluation of a Nanometer Aerosol Differential Mobility Analyzer (Nano-DMA)," *J. Aerosol Sci.*, (in press, 1998).

Chen, D., D. Y. H. Pui and S. L. Kaufman (1995) "Electrospraying of conducting liquids for monodisperse aerosol generation in the 4 nm to 1.8 mm diameter range," *J. Aerosol Sci.*, **26**(6), 963-977.

Cheng, Yung-Sung, Su, Yin-Fong, Yeh, Hsu-Chi, Swift, David L. (1993) "Deposition of Thoron Progeny in Human Head Airways," *Aerosol Sci. Technol.*, **18**, 359-375.

Cheng, Y. S., Yeh, H. C., Guilmette, R. A., Simpson, S. Q., Cheng, K. H., and Swift, D. L. (1996) "Nasal Deposition of Ultrafine Particles in Human Volunteers and Its Relationship to Airway Geometry," *Aerosol Science Technol.*, **25**, 274-291.

Donaldson, K., Gilmour, P., Brown, D. M., Beswick, P. H., Benton, E., and MacNee, W. (1996) Surface free radical activity of PM10 and ultrafine titanium dioxide: a unifying factor in their toxicity. Paper presented at the Eighth International Symposium on Inhaled Particles (Cambridge, UK in August 1996), to be published *in Inhaled Particles VIII* (Ed. T. L. Ogden), Pergamon Press.

Endo, Y., Ono, M., Yamada, T., Kawamura, H., Kobara, K., Kawamura, T., (1996) "Study of Antireflective and antistatic coating with ultrafine particles," *Advanced Powder Technology*, **7**, 131-140.

Ferin, J. (1994) "Pulmonary Retention and Clearance of Particles," *Toxicology Letters*, **72**, 121-125.

Ferin, J. Oberdorster, G., Penney, D. P., Soderholm, S. C., Gelein, R., Piper, H. C., (1990) "Increased pulmonary toxicity of ultrafine particles I. Particle Clearance, translocation, morphology," *J. Aerosol Sci.*, **21**, 381-384.

Ichitsubo, H., T. Hashimoto, M. Alonso, and Y. Kousaka (1996) "Penetration of ultrafine particles and ion clusters through wire screens," *Aerosol Sci. Technol.*, **24**, 119-127.

Kofman, R., Cheyssac, P., Aouaj, A., Lereah, Y., Deutscher, G., Ben-David, T., Penisson, J. M., Bourret, A., (1994) "Surface Melting Enhanced by Curvature Effects," *Surface Science*, **303**, 231-246.

Lin, H., Hsu, C. M., Yao, Y. D., Chen, Y. Y., Kuan, T. T., Yang, F. A., Tung, C. Y., (1995) "Magnetic study of both nitrided and oxidized Co particles," *Nanostructured Materials.*, **6**, 977-980.

Oberdorster, G., Ferin, J., Finkelstein, J., Baggs, R., Stavert, D. M., Lehnert, B. E., (1992) "Potential Health Hazards from Thermal Degradation Events: Particulate vs. Gas Phase Effects," *SAE Technical Paper Series*, Publ. By SAE, Warrendale, PA, USA, 921388, 1-15.

Oberdorster, G., Ferin, J., Lehnert, B. E., (1995) "Correlation between Particle Size, in Vivo Particle Persistence and Lung Injury," *Environmental Health Perspectives*, **102**, (Suppl. 5), 173-179.

Wang, H. and Kasper, G. (1991) "Filtration of efficiency of nanometer-size aerosol particles," *J. Aerosol Sci.*, **22**(1), 31-41.

BIOPHYSICAL DIRECTED ASSEMBLY OF NANOTRUCTURES FOR NEUROCOMPUTING

J.C. Wells[1], L. Maya[2], K. Stevenson[3], T.G. Thundat[3], J. Barhen[1], Y. Braiman[1], and V. Protopopescu[1]

Center for Engineering Science Advanced Research
[1]Computer Science and Mathematics Division
[2]Chemical and Analytical Sciences Division
[3]Life Sciences Division
Oak Ridge National Laboratory, Oak Ridge, Tennessee 37831-6355

ABSTRACT

This paper reports progress in the development of a quantum-dot array that can be operated at room temperature for carrying out nontrivial and innovative computations. We discuss the actual fabrication of 2-nm metal clusters to serve as the quantum dots, device architecture, device simulation, and the development of a computational model. Innovative and unconventional paradigms underlie the different stages of this work. For example, regular array geometry is achieved by directing appropriately derivatized metal clusters to preselected locations along a stretched strand of an engineered DNA sequence. The proposed applications include the implementation of neuromorphic algorithms for pattern recognition.

INTRODUCTION

Emerging revolutionary advances in nanoscale computing, communication, detection, and sensing, subsume a profound understanding of the complex dynamics and properties of small arrays of quantum structures, including quantum dots (QD), ultrasmall Josephson junctions, quantum-dot lasers, and others. Such arrays produce robust bi-stable and multi-stable behavior, which can be exploited for unconventional, yet powerful computational concepts, e.g., neuromorphic computing. Obtaining lattice architectures of sufficient size and regularity to perform actual computations at room temperature has been a formidable challenge, unsurmounted to date. Our objective here is to apply innovative biophysical assembly techniques to overcome this challenge. In particular, appropriately derivatized and passivated gold clusters (i.e., "quantum dots") can be directed to preselected locations along stretched strands of engineered DNA sequences to produce an operational device. Controlling the placement of the clusters with subnanometer precision will enable the electron-transport properties of the array to be engineered precisely at the scale where they are determined. Our effort includes the actual synthesis of quantum dots approximately 2 nm in size, directed self-assembly of a 1D quantum-dot array via DNA templates, device simulation, and development of a computational model.

SYNTHESIS OF GOLD CLUSTERS

We have carried out the synthesis of colloidal gold clusters of core size less than 3-nm by a variety of strategies with appropriate organic coatings. A passivating coating provides a dual function. It provides a barrier for cluster growth as well as functional chemical groups for attachment to DNA nucleotides. This designed propensity for the functionalized gold cluster to bind with a nucleotide is used to assemble the nanoparticle at prescribed locations along an engineered DNA strand. Nanometer-sized metal clusters are a leading candidate for the implementation of single-electron devices at room temperature.

The strategy described here for attaching the cluster to a DNA molecule involves synthesizing gold clusters coated in hydrocarbons terminated with carboxylic-acid functionality. The carboxylic acid is made to react with thymine bases modified with amino groups (see below). Specifically, we have prepared gold colloids, which are thiol-bound to 12-carbon aliphatic hydrocarbons. This was accomplished by a procedure that involves the use of polyamido dendrimers [1], (see Fig.1). These centro-symmetric polymers act as a "nanoreactor" to confine metal ions in the cavity of the polymer. The complexed metal ions are then reduced to the charge-neutral state by means of a chemical reductant such as borohydride. In this particular case, an intermediate step is required because the dendrimer has insufficient affinity for gold ions. This step involves complexation of copper ions, which are then reduced to the metal and subjected to electroless displacement with gold ions. This displacement is feasible because gold is more noble than copper. At this point, the gold cluster must be functionalized with the carboxylic acid and the dendrimer eliminated. This is accomplished by treating an aqueous/tetrahydrofuran solution of the gold-dendrimer complex with 12-mercaptododecanoic acid and subjecting the resulting suspension to solvent extraction with toluene. The desired product, free of dendrimer, is isolated at the interface as an insoluble film, which can be solubilized in dimethylformamide. By this procedure, we have implemented the synthesis and electrophoretic separation of passivated gold clusters. Measurements of the cluster-size distribution from preliminary results show a mean diameter of approximately 2 nm with a standard deviation of 30%.

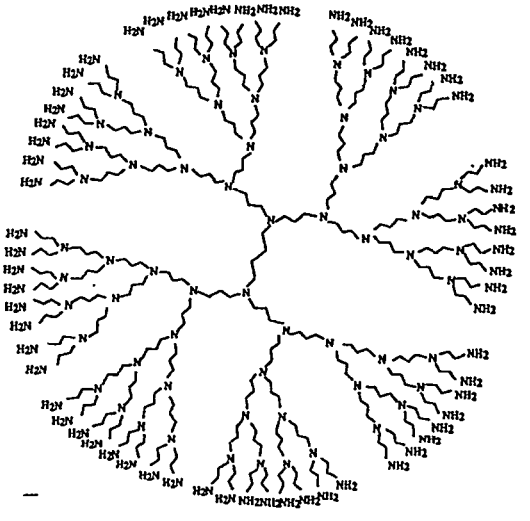

Figure 1. Polyammido dendrimers are centro-symmetric polymers that act as a "nanoreactor" in confining metal ions in cluster synthesis.

DNA TEMPLATES

The need to produce regular arrangements of nanoparticles led to the idea of using DNA as a scaffold or template for assembly of nanoscale arrays. Beginning in the 1980's, Seeman and coworkers experimented with combining DNA fragments to produce regular geometrical shapes. To date they have succeeded in producing a variety of DNA structures, including cubes [2], triangles [3], and truncated octahedrons [4]. They have also produced two-dimensional arrays [5,6] and various forms of DNA knots [7,8]. Using DNA as a structural or template molecule has the following advantages. DNA can be synthesized using any sequence and in any length from one to several hundred nucleotides. (The length along the DNA molecule of a single nucleotide is 0.34 nm.) DNA can be joined end to end to produce longer linear molecules or more complex shapes. It can be modified at predetermined sites to allow for the attachment of other molecules in a specific manner with subnanometer resolution. It can be cut at specific sequences and can be easily degraded when its role in assembly is complete.

Taking advantage of these properties of DNA, we have created linear arrays of DNA with binding sites located at periodic intervals for functionalized gold clusters. As a first step, we designed a single stranded DNA template with modified thymines located every 11 bases. These thymines, modified with amino groups, allow attachment of the nanoparticles at specific sites along the DNA strand through peptide bonds with carboxylic-acid functionalities (see previous section). The complementary DNA strand was synthesized and annealed to the modified strand to produce a double-stranded DNA molecule. The double-stranded DNA was then ligated to produce DNA of various lengths. Strands of the desired length can be isolated using gel electrophoresis to use for specific purposes. After ligation, the carboxyl-acid functionalized gold was bound to the amino groups on the thymine bases using 1-ethyl-3-(3-dimethylaminopropyl)carbodiimide and N-hydroxysuccinimide [9]. The DNA-gold complex was precipitated with ethanol and washed, releasing the free gold. We analyzed the products using gel electrophoresis for purposes of size selection, and using transmission electron microscopy (TEM), Fig. 3. For purposes of the TEM analysis, the DNA-gold complex was coated with cytochrome C and stained with uranyl acetate to facilitate the visualization of DNA. In summary, we have engineered and produced DNA templates up to 200 nm long containing about 60 binding sites for gold clusters. We are refining our procedures to ensure that every binding site along the strand is occupied with a gold cluster and that each cluster is bound to only one DNA strand. Future work will involve the extraction of a single strand of DNA with the gold and attachment to electrodes for measurements of the current-voltage (i.e., $I(V)$) characteristics of the array.

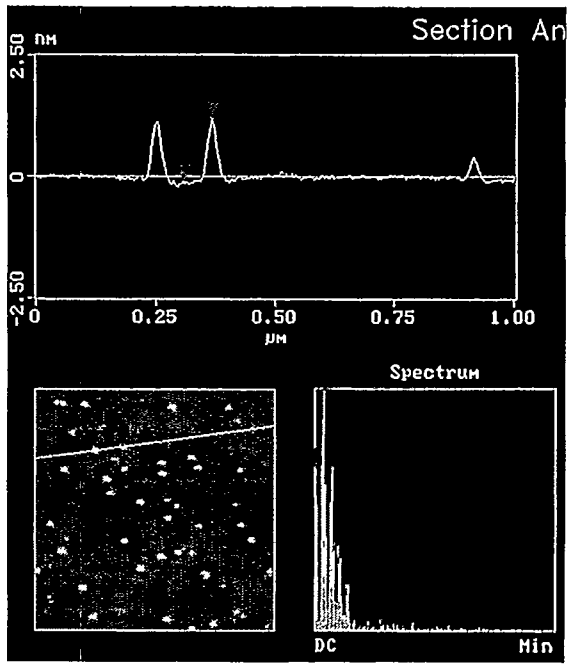

Figure 2. AFM image of gold clusters. The measurement of the cluster height provides accurate information. The width measurement is distorted by the size of the AFM tip.

ELECTRODE CONSTRUCTION

Operating the quantum-dot array as an electronic device requires placing the QDs between two electrodes, with the electrodes coupling to the array via electron tunneling. This alone is a challenging task, as the electrodes are the objects that span the gap between the nanoscopic and macroscopic domains. Using our currently available facilities, electrodes can be fabricated with separation of approximately 20 nm using a focused-ion beam (FIB). In the near future, we anticipate having available an electron-beam facility, which may also be applied to the fabrication of electrodes.

The DNA-gold complex can be stretched between the electrodes to provide electrical connectivity to the quantum-dot array [10]. A thiol group will modify one end of the DNA. A drop of DNA in solution can be placed between the electrodes using a micro-positioner. The drop size will be much larger than the gap width of the electrodes. Since the electrodes are made of gold, the thiol-modified end of DNA will attach to both gold electrodes. These anchored DNA molecules can be stretched under DNA buffer solution using hydrodynamic forces. It is also possible to use an electric field to achieve orientation of the DNA molecules between electrodes. Drying the DNA molecules can cause alterations in structure and orientation due to a variety of effects. Using the technique of critical point drying [11,12] can

preserve the geometry of the stretched DNA. The resulting QD structures can be visualized using an AFM. If more than one DNA strand is stretched between the electrodes, the AFM can be used to selectively dissect unwanted DNA strands.

The DNA strand may act as conduit for leakage currents, and should be removed, but without removing or modifying the gold clusters. One might consider heat treatment for this task, but heat treatment is likely to result in rearrangement of the quantum-dot-array geometry, and can also affect the electrodes due to diffusion. We will utilize a novel UV-Ozone technique that will chip away the DNA molecules without affecting the position of the electrodes or the clusters. The UV-Ozone technique involves exposing organic molecules (such as DNA) to 180-nm UV light. The UV light creates ozone from oxygen, which oxidizes the carbon containing molecules to carbon monoxide, which readily leaves the surface.

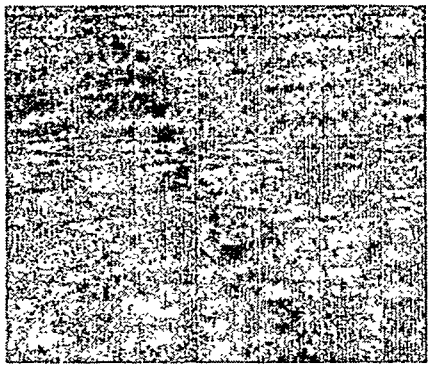

Figure 3. TEM image of DNA-gold complex.

SINGLE-ELECTRON TUNNELING IN QUANTUM-DOT ARRAYS

Consider a one-dimensional array of N tunnel junctions constructed from metallic source and drain electrodes weakly coupled to a linear array of $N-1$ metal clusters. We review the results of the "orthodox theory" of single-electron tunneling [13] to describe the charge transport through the array under small, but finite, bias voltage. (We are interested in nanometer-sized metal clusters in which the Coulomb blockade of conductance may be observed at room temperature, but for simplicity here we neglect any discreteness in the density of electronic states in the cluster resulting from their small size.) The vector $\vec{n}$ defines the state of our system, $\vec{n} \equiv (n_1, \cdots, n_i, \cdots, n_{N-1})$, where n_i is the number of excess electrons accommodated by the i^{th} quantum dot. The Gibbs free energy $E(\vec{n},V)$ describing the electrostatic energy of the array of quantum dots and its interaction with the external voltage is

$$E(\vec{n},V) = \frac{1}{2}\sum_{i=1}^{N-1} C_{ii}\phi_i^2 + \frac{1}{2}\sum_{i=1}^{N}\sum_{j=0,j\neq i}^{N} C_{ij}\left(\phi_i - \phi_j\right)^2 - V_s Q_s - V_d Q_d, \tag{1.1}$$

where $C_{ij} = C_{ji}$ is the mutual capacitance between conductors i and j, ϕ_i is the electrical potential of cluster i measured with respect to the substrate. The source and drain electrodes are enumerated $i = 0$ and $i = N$, respectively. The source potential is $\phi_0 = V_s = V/2$, and the drain potential is $\phi_N = V_d = -V/2$. V is the transport voltage across the array. The charge on the source electrode is $Q_s = C_{01}(\phi_0 - \phi_1) + en_s$, and the charge on the drain electrode is $Q_d = C_{N-1,N}(\phi_N - \phi_{N-1}) + en_d$, where $n_s\,(n_d)$ is the number of electrons that has tunneled from the source (drain) electrode through the first (last) junction.

To determine the free energy, the potentials $\vec{\phi} = (\phi_1, \cdots, \phi_{N-1})$ must be determined from the static charge configuration. Using the charge conservation law, the total charge on island i can be written in terms of the potentials,

$$q_i = C_{ii}\phi_i + \sum_{i=0,i\neq j}^{N} C_{ij}\left(\phi_i - \phi_j\right)^2 = en_i + q_{0,i}, \quad i = 1, \cdots, N-1. \tag{1.2}$$

The background charges $-e/2 < q_{0,i} < +e/2$ are due to incompletely screened charges in the environment of the islands. Equation (1.2) can be written in matrix form $\vec{Q} = \underline{C}\vec{\phi}$, where the generalized capacitance matrix elements are defined

$$\underline{C}_{ii} \equiv \sum_{j=0}^{N} C_{ij}; \quad \underline{C}_{ij} = -C_{ij}, \tag{1.3}$$

and the augmented charge vector is defined $Q_i \equiv q_i + C_{i0}\phi_0 + C_{iN}\phi_N$. The generalized capacitance matrix can be inverted to obtain the potential distribution given any charge distribution. For convenience, we rewrite the free energy of the array using matrix notation as

$$E(\vec{n},V)=\frac{1}{2}\vec{Q}^T\underline{C}^{-1}\vec{Q}-V_sQ_s-V_dQ_d\,. \tag{1.4}$$

In describing the electron transport through the array, we neglect here the effects of co-tunneling, and consider only single-electron tunneling between nearest neighbors in the array. That is, the final state $\vec{m}$ of the tunneling differs from the initial state $\vec{n}$ by the transfer of a single electron though the k^{th} junction, e.g., $\vec{m}=\vec{n}\pm\Delta\hat{u}_k$, where $\Delta\hat{u}_k\equiv\hat{u}_k-\hat{u}_{k-1}$ and $\hat{u}_k$ is a unit vector for the k^{th} quantum dot. The $\pm$ sign gives the direction of tunneling through the junction. If the transition rates are sufficiently small, one can perform a calculation using Fermi's Golden Rule to obtain [13]

$$\Gamma_k^{\pm}(\vec{n},V)=\Gamma_k^{\pm}\left(\Delta E_k^{\pm}(\vec{n},V)\right)=\frac{-\Delta E_k^{\pm}}{e^2R_k}\left[1-\exp\left(\frac{\Delta E_k^{\pm}}{k_BT}\right)\right]^{-1} \tag{1.5}$$

where $\Delta E_k^{\pm}(\vec{n},V)\equiv E(\vec{n}\pm\Delta u_k,V)-E(\vec{n},V)$ is the change in the free energy of the system due to the tunneling, R_k is the effective resistance of the tunnel junction, $e>0$ is the fundamental unit of charge, and the thermal energy is k_BT. One can use probability conservation to write the corresponding master equation describing the time evolution of the probability $P(\vec{n},t)$ of finding the circuit in the state $\vec{n}$

$$\frac{dP(\vec{n},t)}{dt}=\sum_k\left[\Gamma_{k-1}^{+}(\vec{n}-\Delta\hat{u}_{k-1})P(\vec{n}-\Delta\hat{u}_{k-1},t)+\Gamma_k^{-}(\vec{n}+\Delta\hat{u}_k)P(\vec{n}+\Delta\hat{u}_k,t)\right]-\sum_{k=1}^{N}\left[\Gamma_k^{+}(\vec{n})+\Gamma_k^{-}(\vec{n})\right]P(\vec{n},t). \tag{1.6}$$

Practical approaches to solving the master equation are described in Refs. [14-15]. Given the solution, the average tunneling current is given by computing the net flow through any junction k in the array:

$$I(V)=I_k(V)=e\sum_{\vec{n}}P(\vec{n})\left[\Gamma_k^{+}(\vec{n},V)-\Gamma_k^{-}(\vec{n},V)\right]. \tag{1.7}$$

Since the summation is performed over the charge states, the current is a function of the transport voltage.

NEUROMORPHIC ALGORITHMS FOR COMPLEX INFORMATION PROCESSING

Quantum dot nanoelectronic devices represent a promising hardware technology that offers both conceptual opportunities and engineering challenges for complex information processing applications. One such application, pattern recognition, is of considerable interest to the development of modern intelligent systems and will be considered here. In recent years, the quest for innovative approaches to machine intelligence has received considerable attention. The proven ability of neuromorphic algorithms to deal with uncertain information and to interact with dynamic environments is therefore providing a strong incentive to explore the feasibility of their implementation on arrays of quantum dots. However, in contrast to conventional hardware approaches, we must develop here computational paradigms that exploit from the onset not only the concept of massive parallelism but also, and most importantly, the physics of the underlying device.

Artificial neural networks are adaptive systems that process information by means of their response to discrete or continuous input [16]. Neural networks can provide practical solutions to a variety of artificial intelligence problems, including pattern recognition [17], autonomous knowledge acquisition from observations of correlated activities [18], real-time control of complex systems [19], and fast adaptive optimization [20]. At the heart of such advances lies the development of efficient computational methodologies for "learning" [21]. The development of neural learning algorithms has generally been based upon the minimization of an energy-like neuromorphic error function or functional [22]. Gradient-based techniques have typically provided the main computational mechanism for carrying out the minimization process, often resulting in excessive training times for the large-scale networks needed to address real-life applications. Consequently, to date, considerable efforts have been devoted to: (1) speeding up the rate of convergence [23-25] and (2) designing more efficient methodologies for deriving the gradients of these functions or functionals with respect to the parameters of the network [26,27]. The primary focus of such efforts has been on recurrent architectures. However, the use of gradient methods presents challenges even for the less demanding multi-layer feed-forward architectures, which naturally

occur in quantum-dot arrays. For instance, entrapment in local minima has remained one of the fundamental limitations of most currently available learning paradigms. The recent development of the innovative global optimization algorithm TRUST [28] has been suggested [29] as a promising new avenue for addressing such difficulties.

Roychowdhury and his collaborators were the first to propose the implementation of neural networks in terms of quantum-dot arrays [30]. In their *Gedankenexperiment* a generic array of nanometer-sized metallic islands would be deposited on a resonant tunneling diode. Furthermore, all islands would have a direct conductive/capacitive link to their nearest neighbors established, for example via organic molecular wires. They considered both continuous and discrete charge networks. The latter are of interest here. The Roychowdhury team showed that the evolution of an initial charge distribution toward a stable final equilibrium distribution can be given a neuromorphic interpretation and that this property emerges purely as a result of the discreteness of the electronic charge [31]. There are several shortcomings in their proposal. First, they assumed that all inter-island capacitance could be modified arbitrarily, but offered no mechanism to achieve this essential property. Moreover, their architecture involved capacitive coupling between all islands, a "*floating*" plate, and a grounded plate. Tunneling is assumed to occur only between the islands and the floating plate, but not between islands. Thus, even though their paradigm would allow some elementary form of combinatorial optimization, it could not be used for neural learning needed in pattern recognition.

In the previous section we have illustrated the underlying physical concepts of single-electron transport in arrays of quantum dots. As pointed out by Roychowdhury and coworkers [30-31], there is a profound similarity between the dynamics of neural networks and that of quantum-dot arrays. In the latter, the free energy of an array characterized by a charge distribution can be lowered in terms of tunneling events. For neural networks, on the other hand, Hopfield has shown that the stable states of the network are the local minima of a bounded Lyapunov function of the net's output parametrized by the synaptic interconnection weights. A careful analysis, however, reveals that this formal similarity is not adequate for implementing learning algorithms for pattern recognition. By comparing the leading terms of the free energy in Eq. (1.4), i.e., $\frac{1}{2}\bar{Q}^T\underline{C}^{-1}\bar{Q}$ and the Lyapunov function in a Hopfield network, i.e., $L(x,\underline{W}) = -\frac{1}{2}x^T\underline{W}x$, we see that the inverse of the augmented capacitance matrix would have to play the role of the synaptic matrix. However, the elements of $\underline{C}_{ij}$ are *fixed*, and cannot be modified. An alternative approach for controlling the dynamics of the system has to be found. In principle, one could manipulate the free energy of the array via capacitive gating of each of the quantum dots. However, for an array of quantum dots 1 to 2 nm in size, which is necessary for room temperature operation, we are not aware of technology capable of implementing such gating on a nanometer scale.

Studies of the dynamics of arrays of quantum dots in the presence of the time-dependent excitation (e.g., RF signal [33,34]) reveal a rich structure of dynamical behaviors that offers a tremendous potential for performing the computation we need. In particular, a team led by Oosterkamp has recently made available an extensive survey of experiments and methods for photon-assisted tunneling in quantum dots [35]. In the absence of a time-dependent field, current flows through a quantum dot via tunneling when an unoccupied internal energy state is aligned to the Fermi energy of the leads. However, as pointed out by Oosterkamp *et al* following seminal work by Likharev *et al.*, if a time-varying AC voltage $A_0\cos(2\pi\omega t)$ is applied, inelastic tunnel events are induced when electrons exchange photons of energy $h\nu$ with the oscillating field. Tien and Gordon first described theoretically this phenomenon of multiphoton-assisted tunneling [36]. A direct inclusion of this phenomena in a master equation that takes into account Coulomb blockade can be made by writing the tunneling rate $\bar{\Gamma}$ through each barrier in the presence of an electromagnetic excitation in terms of the rates without the external AC field,

$$\bar{\Gamma}_k^{\pm}(\vec{n},V,A_0,\nu) = \sum_{\alpha=-\infty}^{\infty} J_\alpha\left(\frac{eA_0}{h\nu}\right)\Gamma_k^{\pm}(\Delta E_k^{\pm} + \alpha h\nu) \tag{1.8}$$

where J_α denotes the Bessel function of the first kind and α denoting the number of photons exchanged. This generalized master equation is obtained by substituting the rates in Eq. (1.8) into Eq. (1.6). The current through this device is a function of the transport voltage V, and the amplitude A_0 and frequency ν of the AC field,

$$I(V,A_0,\nu)=e\sum_{\vec{n}}P(\vec{n})\left[\bar{\Gamma}_k^{+}(\vec{n},V,A_0,\nu)-\bar{\Gamma}_k^{-}(\vec{n},V,A_0,\nu)\right]. \tag{1.9}$$

We will consider the transport voltage V as the input variable and the current I as the output function in implementing neuromorphic computation. For a two-dimensional quantum-dot array with K input and K output nodes, we can readily generalize the description given here to consider K input voltages V_k and K output currents $I_k(V_k,A_0,\nu)$ (see Fig. 4). This vector-valued function $\mathbf{I}_K$ is controllable through the parameters of the external, alternating field, A_0 and ν, by minimizing the error function $\mathcal{E}$, defined over the number of L training patterns as the squared difference between the observed currents, $\mathbf{I}_K$ and the target currents, $\mathbf{I}^*_K$, (see below),

$$\mathcal{E}\equiv\frac{1}{L}\sum_{l=1}^{L}\left[\mathbf{I}_K(\mathbf{V}_K,A_0,\nu)-\mathbf{I}_K^*\right]^2. \tag{1.10}$$

For convenience, matrix and vector dimensions are explicitly indicated as subscripts. If a larger number of controls are necessary, then a polychromatic AC field may be implemented as the global control, rather than a monochromatic field.

The pattern recognition scheme can now readily be implemented using the following method. We assume that two sets of L vectors are used for training. They are stored as rows of two matrices $\mathbf{\Omega}_{LI}$ and $\mathbf{R}_{LO}$ respectively, which represent the input signal patterns and the target outputs. We denote the number of columns of each matrix as I for input and O for output, without confusion. Since typically $L >> I$, two preprocessing steps are used [25]. First, clustering is used to transform $\mathbf{\Omega}_{LI}$ and $\mathbf{R}_{LO}$ into $\mathbf{\Omega}^*_{KI}$ and $\mathbf{R}^*_{KO}$. Then, two successive *nonlinear* transformations map $\mathbf{\Omega}^*_{KI}$ into $\mathbf{H}_{KK}$, a nonsingular K x K presynaptic matrix, which constitutes the actual input into the quantum-dot array. We also decouple the nonlinearity of the transfer function, φ, at the output layer of the neural net from the linear interlayer pattern propagation mediated by the synaptic weights $\mathbf{W}_{KO}$. This transformation is used to compute the postsynaptic input to the output layer of the neural net as a K x O rectangular matrix. Since the latter is connected via a bijective sigmoid mapping to the output training examples, the synaptic interconnection matrices $\mathbf{W}_{KO}$ can be determined by solving the linear system $\mathbf{H}_{KK}\ \mathbf{W}_{KO}=\varphi^{-1}(\mathbf{R}^*_{KO})$ using gradient iteration. In simulation on a conventional computer, this can be accomplished by exactly solving a system of linear equations using singular-value decomposition techniques. On nanoelectronic hardware, this will be achieved by directly optimizing the error function in Eq. (1.10) in terms of the parameters of the external field, A_0 and ν. If the dimensions O of the output pattern is smaller than the number K of output nodes of the quantum-dot array, the output error is calculated using the O dimension in the Euclidean distance.

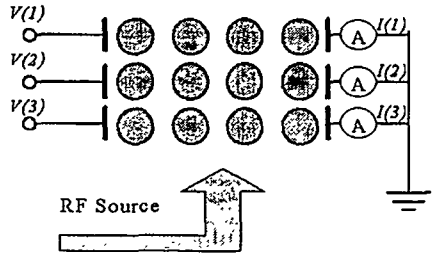

Figure 4. Two-dimensional QD array showing voltages as input channels and currents as outputs.

In this minimization process, we can directly account for uncertainties to obtain best estimates for the device parameters and responses of interest. For example, nominal values for the elements of the capacitance matrix will be computed from "first-principles" simulations of the metal clusters and substrate via density-functional-theory-based molecular dynamics [37] and the current through the device will be computed via numerical solutions to the master equation [14,15]. To obtain best estimates for critical parameters (e.g., A_0 and ν), we must consistently combine computational results and experimental measurements. We achieve this by optimizing a generalized Bayesian loss function that simultaneously minimizes the differences between the best estimate responses and the measured responses on one hand, and the best estimate and calculated parameters on the other hand. Our optimization process uses the inverse of a generalized total covariance matrix as the natural metric of the calculational manifold in conjunction with response sensitivities to all parameters [38].

ACKNOWLEDGMENTS

Research partially sponsored by the Engineering Research Program of the Office of Basic Energy Sciences, U.S. DOE, and partially by the Laboratory Directed Research and Development Program of Oak Ridge National Laboratory (ORNL), managed by UT-Battelle, LLC for the U. S. DOE under Contract No. DE-AC05-00OR22725. The authors wish to express gratitude for the assistance of Dr. Muralidharan Govindarajan for assistance with the TEM analysis.

REFERENCES

1. M. ZHAO and R.M. CROOKS, "Intradendrimer Exchange of Metal Nanoparticles," *Chem. Mater.* **11**, 3379 (1999).
2. J. CHEN *et al.*, "Synthesis from DNA of a Molecule with the Connectivity of a Cube," *Nature*, **350**, 631 (1991).
3. J. QI, *et al.*, "Ligation of Triangles Built from Bulged 3-Arm DNA Branched Junctions," *J. Am. Chem. Soc.* **118**, 6121 (1996).
4. Y. ZHANG and N.C. SEEMAN, "Construction of a DNA-Truncated Octahedron," *J. Am. Chem. Soc.*, **116**, 1661 (1994).
5. X. LI, X. YANG, J. QI, and N.C. SEEMAN, "Antiparallel DNA Double Crossover Molecules as Components for Nanoconstruction," *J. Am. Chem. Soc.* **118**, 6131 (1996).
6. E. WINFREE, *et al.*, "Design and Self-Assembly of Two-Dimensional DNA Crystals," *Nature* 394, 539, (1998).
7. J.E. MUELLER, *et al.*, "Design and Synthesis of a Knot from Single-Stranded-DNA," *J. Am. Chem. Soc.* **113**, 6306, (1991).
8. S.M. DU, *et al.*, "The Construction of a Trefoil Knot from a DNA Branched Junction Motif," *Biopolymers*, **34**, 31, (1994).
9. Z. GRABAREK and J. GERGELY, "Zero-Length Crosslinking Procedure with the Use of Active Esters," *Anal. Biochem.* **185**,131, (1990).
10. S. B. SMITH, L. FINZI, and C. BUSTAMANTE, "Direct Mechanical Measurements of the Elasticity of Single DNA-Molecules by Using Magnetic Beads," *Science* **258**, 1122 (1992).
11. T. THUNDAT, D.P. ALLISON, and R. J. WARMACK, "Stretched DNA Structures Observed With Atomic-Force Microscopy," *Nucleic Acids Res.* **22**, 4224 (1994).
12. T. THUNDAT, R. J. WARMACK, D.P. ALLISON, and K.B. JACOBSON, "Critical-Point Mounting of Kinetoplast DNA for Atomic-Force Microscopy," *Scanning Microscopy* **8**, 23 (1994).
13. K.K. LIKHAREV, "Single Electron Devices and their Applications", *Procs. IEEE*, **87**(4), 606-632 (1999).
14. L.R.C. FONSECA, A.N. KOROTKOV, K.K. LIKHAREV, and A.A. ODINTSOV, "A Numerical Study of the Dynamics and Statistics of Single-Electron Systems", *J. Appl. Phys.* **78**, 3238 (1995).
15. A.S. CORDAN, *et al.*, "Optimization of the Master Equation Set for a Multidot Tunnel Structure", *Eur. Phys. J AP* **7**, 137 (1999).
16. M. HASSOUN, *Fundamentals of Artificial Neural Networks*, MIT Press (1995).
17. M. BISHOP, *Neural Networks for Pattern Recognition*, Oxford University Press (1997).
18. M. BECKERMAN, *Adaptive Cooperative Systems*, Wiley Interscience (1997).
19. D. WHITE and D. SOFGE, *Handbook of Intelligent Control: Neural, Fuzzy and Adaptive Approaches*, Van Nostrand Reinhold (1992).
20. A. CICHOCKI and R. UNBENHAUEN, *Neural Networks for Optimization and Signal Processing*, Wiley (1993).
21. P. MARS, J. CHEN, and R. NAMBIAR, *Learning Algorithms*, CRC Press (1996).
22. Y. CHAUVIN and D. RUMELHART, *Backpropagation: Theory, Architectures, and Applications*, Lawrence Erlbaum (1995).
23. J. BARHEN, *et al.*, "Neural Learning of Constrained Nonlinear Transformations", *IEEE Computer*, **22**(6), 67-76 (1989).
24. N. TOOMARIAN and J. BARHEN, "Fast Temporal Neural Learning Using Teacher Forcing", *U.S. Patent No. 5,428,710* (March 28, 1995).
25. J. BARHEN, R. COGSWELL, and V. PROTOPOPESCU, "Single Iteration Training Algorithm for Multi-layer Feed-forward Neural Networks," *Neural Proc. Lett*, **11**(2) (in press, 2000).
26. J. BARHEN, *et al.*, "Applications of Adjoint Operators to Neural Networks", *Appl. Math. Lett.*, **3**(3), 13-18 (1990).
27. N. TOOMARIAN and J. BARHEN, "Neural Network Training by Integration of Adjoint Systems of Equations Forward in Time", *U.S. Patent No.* 5,930,781 (July 27, 1999).
28. J. BARHEN, V. PROTOPOPESCU, and D. REISTER, "TRUST: A Deterministic Algorithm for Global Optimization", *Science*, **276**, 1094-1097 (1997).
29. A. SHEPHERD, *Second-Order Methods for Neural Networks*, Springer (1997).
30. V. ROYCHOWDHURY *et al*, "Collective Computational Activity in Self-Assembled Arrays of Quantum Dots: Novel Neuromorphic Architectures for Nanoelectronics", *IEEE Trans. Electron. Devices* **42**(10), 1688-1698 (1996).
31. S. BANDYOPADHYAY and V. ROYCHOUDHURY, "Computational Paradigms in Nanoelectronics: Quantum Coupled Single Electron Logic and Neuromorphic Networks", *Jap. Jour. Applied Phys.*, **35**(6), 3350-3362 (1996).
32. J.A MELSEN, *et al.*, "Coulomb Blockade Threshold in Inhomogeneous One-Dimensional Arrays of Tunnel Junctions," *Phys. Rev. B* **55**, 10638 (1997).
33. L. P. KOUWENHOVEN *et al*, "Quantized Current in a Quantum-Dot Turnstile Using Oscillating Tunnel Barriers", *Phys. Rev. Lett.* **67**, 1626-1629 (1991).
34. M. N. WYBOURNE *et al*, "Coulomb-Blockade Dominated Transport in Patterned Gold-Cluster Structures", *Jap. Jour. Appl. Phys.*, **36**, 7796 (1997).
35. T. OOSTERKAMP *et al*, "Photon Assisted Tunneling in Quantum Dots", *arXiv:cond-mat/9904359*, LANL (26 April 1999).
36. P.K. TIEN and J.P. GORDON, "Multiphoton Process Observed in the Interaction of Microwave Fields with the Tunneling between Superconductor Films," *Phys. Rev.* **129**, 647 (1963).
37. P. BALLONE and W. ANDREONI, "Density Functional Theory and Car-Parrinello Molecule Dynamics for Metal Clusters," in *Metal Clusters*, Ed. W. Ekardt, (Wiley, 1999).
38. J. BARHEN and V. PROTOPOPESCU, "Ultrafast Neural Network Training for Robot Learning from Uncertain Data", in *Distributed Autonomous Robotic Systems*, L. Parker ed., Springer (in press, 2000).

EXPERIMENTAL AND THEORETICAL ASPECTS OF QUANTUM TELEPORTATION

Lei Zhang, Jacob Barhen, and Hua-Kuang Liu

Center for Engineering Science Advanced Research
Computer Science and Mathematics Division
Oak Ridge National Laboratory
Oak Ridge, TN 37831-6355, USA
zhangl@ornl.gov, barhenj@ornl.gov, and 9hl@ornl.gov

ABSTRACT

We present a short summary of progress achieved at the Center for Engineering Science Advanced Research (CESAR) of the Oak Ridge National Laboratory (ORNL) in the recently initiated Quantum Teleportation project. The primary objective of this effort is to study the signaling potential of quantum information processing systems based on quantum entanglement. Our initial effort has focused on the development and demonstration of a novel, ultra-bright EPR source, based upon the innovative concept of cascaded type-II optical parametric downconversion. The main features of this source are analyzed, and results of a multi-photon entanglement experiment are presented. Theoretical challenges for superluminal communications are also highlighted.

I. INTRODUCTION

In recent years, there has been increased interest in exploiting the unique capabilities that quantum mechanics offers for the processing of information. In that context, quantum teleportation (QT) is a particularly attractive paradigm. It involves the transfer of an unknown quantum state over an arbitrary spatial distance by exploiting the prearranged entanglement (correlation) of "carrier" quantum systems in conjunction with the transmission of a minimal amount of classical information. This concept was first discussed by Aharonov and Albert (AA) using the method of nonlocal measurements [1].

Over a decade later, Bennett, Brassard, Crepeau, Jozsa, Peres, and Wooters (BBCJPW) developed a detailed alternate protocol for teleportation [2]. It consists of three stages. First, an Einstein-Podolsky-Rosen (EPR) [3] source of entangled particles is prepared. Sender and receiver share each a particle from a pair emitted by that source. Second, a Bell-operator measurement is performed at the sender on his EPR particle and the teleportation-target particle, whose quantum state is unknown. Third, the outcome of the Bell measurement is transmitted to the receiver via a classical channel. This is followed by an appropriate unitary operation on the receiver's EPR particle. To justify the name "*teleportation*", BBCJPW note that the unknown state of the transfer-target particle is destroyed at the sender site and instantaneously appears at the receiver site. Actually, the state of the EPR particle at the receiver site becomes its exact replica. The teleported state is never located between the two sites during the transfer.

A number of exciting theoretical developments has appeared since the publication of the AA and BBCJPW protocols. For instance, Vaidman has shown [4] how nonlocal measurements can be used for

the teleportation of the unknown quantum states of systems with continuous variables. In AA, nonlocal refers to measurements that cannot be reduced to a set of local measurements; for example, the measurement of a sum of two variables related to two separated spatial locations. He was also the first to suggest a method for two-way teleportation. Braunstein and Kimble extended Vaidman's analysis to incorporate finite degrees of correlation among the relevant particles and to include inefficiencies in the measurement process [5]. In their proposed implementation of QT of continuous quantum variables, the entangled state shared by sender and receiver is a highly squeezed two-mode state of the electromagnetic field, with the quadrature modes of the field playing the roles of position and momentum. Stenholm and Bardroff have generalized the BBCJPW protocol to systems of arbitrary dimensionality [6]. Zubairy has considered the teleportation of a field state (a coherent superposition of 2^n Fock states) from one high-Q cavity to another [7]. In the previously cited studies, QT dealt with "*intraspecies*" teleportation e.g., photon-to-photon. Maierle, Lidar, and Harris were recently the first to introduce an "*interspecies*" teleportation scheme [8]. Specifically, in their proposal, the information contained in a superposition of molecular chiral amplitudes is to be teleported to a photon. Finally, let us mention that Brassard, Braunstein, and Cleve have argued [9] that QT is an essential ingredient for quantum computing, and have presented a simple circuit that implements QT in terms of primitive operations in quantum computing.

Let us turn to experimental realizations of QT. The first laboratory implementation of QT was carried out in 1997 at the University of Innsbruck by a team led by Anton Zeilinger [10]. It involved the successful transfer of a polarization state from one photon to another. A type-II degenerate, pulsed parametric down-conversion process was used to generate the polarization-entangled EPR source. The experimental design is relatively easy to implement. The drawback is that only one of the four EPR-Bell states can be distinguished. In 1998, the Zeilinger team demonstrated that freely propagating particles that never physically interacted with one another could also readily be entangled [11]. In this experiment, one photon each from two pairs of polarization-entangled photons were subjected to Bell-state measurement. As a result, the other two photons were projected into an entangled state. This result is remarkable, since it shows that quantum entanglement does not require entangled particles to originate from a common source or to have interacted in the past. The second QT experiment reported in the open literature in February 1998 was carried out at the University of Rome by a team lead by Boschi and Popescu [12]. It involved a quantum optical implementation. The polarization degree of freedom of one of the photons in the EPR pair was employed for preparing the unknown state. The idea is to exploit the fact that the two degrees of freedom of a single photon can be k-vector entangled. This method cannot, however, be used to teleport an external, unknown quantum state. The conservation of energy and time photon entanglement over distances exceeding 10 km has been demonstrated experimentally [13] using a telecommunications fiber network. In a similar vein, the distribution of cryptographic quantum keys over open space optical paths of approximately 1km was also reported [14].

The potentially enormous economic and national security implications of a successful realization of a loopholes-free QT system has led to an intense competition among the few laboratories that have the experimental capabilities to adequately address this challenge. A particularly "hot" topic is to demonstrate which scheme is more "*complete*" [15] or more "*unconditional*" [16]. However, Vaidman has proved that reliable QT can not be achieved using the methods implemented in the experiments reported to date [17]. Specifically, it is impossible to perform complete Bell operator measurements without using interaction between the quantum states of the particles.

Our purpose in this paper is to present a short summary of progress achieved at the Center for Engineering Science Advanced Research (CESAR) of the Oak Ridge National Laboratory (ORNL) in a recently initiated QT project. The primary objective of this effort is to study the signaling potential of quantum information processing systems based on quantum entanglement. Our initial effort has focused on the development of an ultra-bright EPR source. This has been accomplished successfully, and is discussed in Section II. The theoretical challenges are highlighted in Section III. Near-term objectives (e.g., multi-channel quantum teleportation employing multi-particle, or GHZ photons) and conclusions reached so far are included in Section IV.

II. EXPERIMENTS

The simplest quantum states for QT involve two-level systems, including spin states of a spin ½ particle, the polarization states of a photon, the ground and excited state of an atom or ion, or the Fock states of a microwave cavity. In the following discussion, without loss of generality, we will use polarization states. Before a polarization-entangled photon can be used for QT (including applications such as quantum cryptography or quantum remote sensing), it is essential to characterize the EPR source in detail.

Preparation of entangled photon pairs

The preparation of polarization-entangled photons uses the process of optical parametric down-conversion (OPDC) [18] to produce correlated photon pairs. This process employs a nonlinear medium, which allows pump photons to decay into pairs of photons under the restrictions of energy and momentum conservation. Since the two "decay" photons are created at the same time, the detection of one photon indicates with almost certainty the existence of the other. The conservation of energy and momentum also allows the determination of one photon's wavelength and direction provided the other one's are known. Three phase-matching methods are available for generation of correlated photons. They are referred to as type-I, type-II and cascaded type-I.

In a type-I process, the generated photon pair shares the same polarization. With this method, a broad range of momentum and energy entangled photon pairs can be produced, either in a non-degenerate geometry, such that they have different wavelengths, or in a degenerate geometry, where the two photons share the same wavelength. The limitation of type-I OPDC is that the photons are actually created in polarization product-states, and may not violate a true test of Bell's inequalities. In a type-II process [19], the photon pair is created with orthogonal polarizations. Therefore, as opposed to the type-I source, the photons emitted into two distinct modes are usually not entangled, because they can be distinguished on the basis of their polarization. It was found that, when the cut angle of the crystal is larger than that of the degenerate OPDC (or when the crystal is tilted toward that direction), the two emission cones corresponding to different modes would overlap. In the two directions determined by the cones' intersection the polarization distinguishability disappears. Therefore, such a source can produce polarization-entangled photon pairs. Typical emission patterns of type-I and type-II OPDC are shown in Figure 1. The type-I BBO crystal has a cut angle of 29.6° and was tilted 0.2° (internal) while the type-II BBO crystal has a cut angle of 42.9° and was tilted 2.5° (internal). Detailed explanations are provided in the caption.

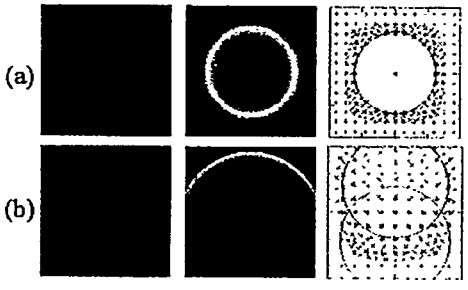

Figure 1 Simulated emission patterns of idler beams (left), signal beams (center) and separations between idler beams ("×") and signal beams ("+") with (a) type-I and (b) type-II phase matched OPDC in a BBO crystal. The pump wavelength is 395 nm. The solid circles correspond to a degenerate case. All patterns are calculated over a 10°×10° solid angle except the top right one, which is calculated over a 4°×4° solid angle.

Figure 2 shows the geometry when the crystal cut angle is larger than that of the degenerate OPDC. Polarization-entangled photon pairs, labeled as *A* and *B*, propagate along the two directions where the cones intersect. The horizontal polarization (→, ordinary) and the vertical polarization (↑, extraordinary) are orthogonal, and the corresponding polarization-entangled two-photon state is given by

$$\left|\psi_{A,B}\right\rangle = \frac{1}{\sqrt{2}}\left(\left|\rightarrow_A, \uparrow_B\right\rangle + e^{i\alpha}\left|\uparrow_A, \rightarrow_B\right\rangle\right) \tag{1}$$

The relative phase α arises from the crystal birefringence, and an overall phase shift is omitted. With the help of additional half wave or quarter wave plates, one can easily produce any of the four EPR-Bell states,

$$\left|\psi^{\pm}_{A,B}\right\rangle = \frac{1}{\sqrt{2}}\left(\left|\rightarrow_A,\uparrow_B\right\rangle \pm \left|\uparrow_A,\rightarrow_B\right\rangle\right), \tag{2}$$

$$\left|\phi^{\pm}_{A,B}\right\rangle = \frac{1}{\sqrt{2}}\left(\left|\rightarrow_A,\rightarrow_B\right\rangle \pm \left|\uparrow_A,\uparrow_B\right\rangle\right). \tag{3}$$

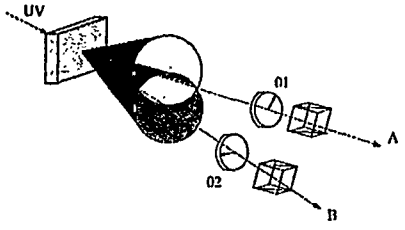

Figure 2 Geometry of a type-II OPDC. Polarization entangled photons are found along the two intersection directions (*A* and *B*) of the two emission cones.

We have already demonstrated type-II OPDC with a femtosecond pump source. The pump laser system is a mode-locked Ti: Sapphire laser (Mira 900-F from Coherent) pumped by an Argon laser (INNOVA Sabre from Coherent). The output gives a 76 MHz pulse train at a wavelength of 790 nm, with 120 femtosecond pulse width and 1.2 watt CW power. The UV beam is generated with a 7-mm thick LBO crystal (from CASIX) cut for second harmonic generation (SHG) at 790 nm. The conversion efficiency from IR to UV is about 40%. After passing through a prism pair for dispersion compensation and fundamental removal, the final UV beam has a pulse width of less than 200 fs and 300 mW power. Figure 3 shows the overlapped photon cones, generated by type-II OPDC. An interference filter with a bandwidth of 2 nm (from Avdover) is placed before the single photon counting module (SPCM-AQR-14 from EG&G Canada). The maximum photon counting rate is 7000 (sec^{-1}) (counted by fiber with background subtracted).

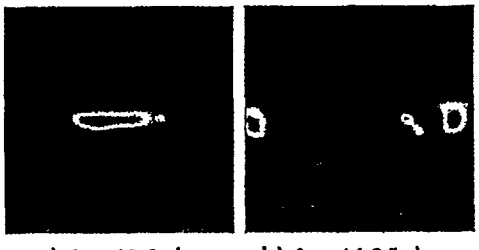

a) θ = 43.0 deg b) θ = 44.25 deg

Figure 3 Emitted photon cones scanned with a 100-μm diameter fiber over a 1 cm × 1 cm area, 6.5 cm behind the crystal's output surface. A 3-mm thick BBO with cut angle of 43° is used for type-II OPDC. An interference filter with bandwidth of 2 nm is placed before the SPCM. a) corresponds to a collinear and b) corresponds to a non-collinear case. θ corresponds to effective internal angle between the optical axis and the pump UV beam direction.

The polarization correlations were measured using the setup shown in Figure 2. With θ_1 set at -45° and θ_2 rotated from -45° to 315°, the coincidence rate from the two detectors was recorded. It corresponds to the $|\psi^+>$ state. Then a half-wave plate was inserted into one of the arms to rotate the polarization by 90° in that arm. The corresponding polarization entanglement was measured and gave the $|\phi^+>$ state. These measurement results can be seen in Figure 4.

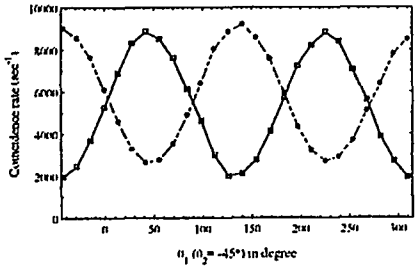

Figure 4 Measurement of the polarization entanglement of an EPR source generated with a type-II phase matched BBO crystal. The solid square corresponds to the $|\psi^+>$ state and the circle corresponds to the $|\phi^+>$ state. The solid line is the fitting with $\sin^2(\theta_1 + \theta_2)$ and the dashed line is the fitting with $\cos^2(\theta_1 + \theta_2)$.

Cascaded Type-I Downconversion Source of Correlated Photons

A new method, that uses the process of OPDC in an innovative geometry involving two type-I crystals, has recently been reported [20]. Two adjacent, relatively thin, nonlinear crystals are operated with type-I phase matching. The identically cut crystals are oriented so that their optic axes are aligned in perpendicular planes. Under such conditions, a 45° polarized pump photon will be equally likely to down convert in either crystal. Generally photons generated by different crystals can be distinguished by their polarizations. This problem was solved by inserting quarter-wave plates behind the crystal pairs. Furthermore, these two possible down-conversion processes are *coherent* with one another.

Cascaded Type-II Optical Parametric Down-conversion

We now present some new experimental results that we have achieved in the short period since the inception of this project. First, we discuss our novel EPR source, which is based on optical parametric down-conversion, but with a cascaded type-II OPDC configuration. It combines the main advantages of, and outperforms previously reported entangled photon generators. Next, we analyze its main features and limitations. Our new source consists of two adjacent thin nonlinear crystals with identically cut angles, which correspond to degenerated type-II phase matching. The two crystals are oriented with their optic axes aligned in opposite direction. A pump photon may be equally down-converted in either crystal, and these two possible downconversion processes generate two pairs of correlated photons (see Figure 5). The advantage of our proposed configuration is obvious. First, the limitation in overlap of idler and signal photons has been greatly relaxed (see Figure 1) compared with the case in cascaded type-I OPDC. Our architecture can thus provide much brighter polarization-entangled photons in either degenerate or non-degenerate cases. Second, the outputs are naturally polarization-entangled. Third, in the directions corresponding to the intersections of the two cones, the two pairs of polarization-entangled photons coincide exactly. By selected alignment, such a source may work as a *four-photon entanglement* source.

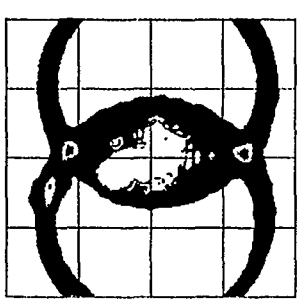

Figure 5 Emitted photon cones generated by type-II OPDC, scanned with a 100-μm diameter fiber over a 1.6 cm × 1.6 cm area, 7.5 cm behind the crystal's output surface. The background has been subtracted. The residual of the UV pump photons at the center has been cropped. The thickness of both BBO crystals is 1-mm and cut at an angle of 43.9°.

The single photon counting modules (SPCM-AQR-14 from EG&G, Canada) that we used have internal amplifiers. For each photon detected, there is a 5 V output signal with 30 ns pulse width. Since the pump source is a mode locked Ti: Sapphire laser with 76 MHz modulation frequency, the separation between pulse trains is 13 ns. Hence, we have used a Quad Constant-Fraction Discriminator (935-CFD from EG&G ORTEC) to compress the output pulse width to 5 ns. The outputs from two CFD output connectors are then routed to a Quad 4-Input Logic Unit (CO4020 from EG&G ORTEC) for coincidence count. The output from CO4020 is sent to a Universal Time Interval Counter (SR620 from Stanford Research Systems). The outputs from the 935-CFD are also sent to a Quad Timer/Counter (974 from EG&G, ORTEC) to record the single counting rate.

Two-photon interferometry for analyzing the entanglement

If one overlaps two photons at a beamsplitter, interference effects determine the probabilities to find the two photons incident one each from A and B either both in one of the two outputs or to find one in each output. Only if two photons are in the state

$$\left|\psi^{-}_{A,B}\right\rangle = \frac{1}{\sqrt{2}}\left(\left|\rightarrow_A,\uparrow_B\right\rangle - \left|\uparrow_A,\rightarrow_B\right\rangle\right), \tag{4}$$

will they leave the beam splitter in different output arms. If one puts detectors there, a click in each of them, i.e. a coincidence, means the projection of the two photons onto the state $|\psi^{-}>$. For the other three Bell states both photons will exit together through one of the two output arms. To register two photons in one output arm additional detectors or a certain detuning of the setup is necessary since these detectors do not distinguish between one or more photons.

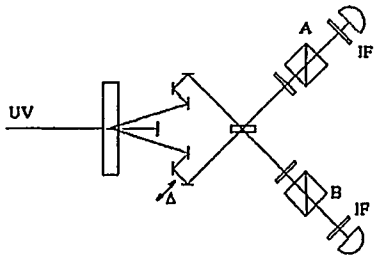

Figure 6 Experimental setup for measurement of entanglement and interference

The experimental results for multi-photon entanglement, obtained using our cascaded type-II OPDC source in the setup shown in Figure 6 above, are illustrated in Figures 7 and 8.

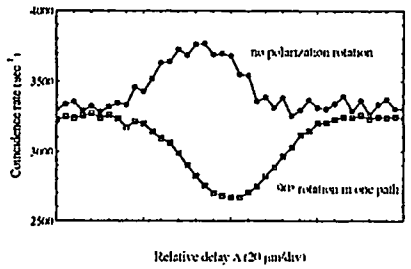

Figure 7 Coincidence rate as a function of the delay between the arrival of photon A and photon B. The lower curve shows the measured destructive interference when the polarization in one path was rotated 90°. The upper curve shows the measured constructive interference with no polarization rotation. It includes a strong *biphoton effect* in our cascaded type-II OPDC.

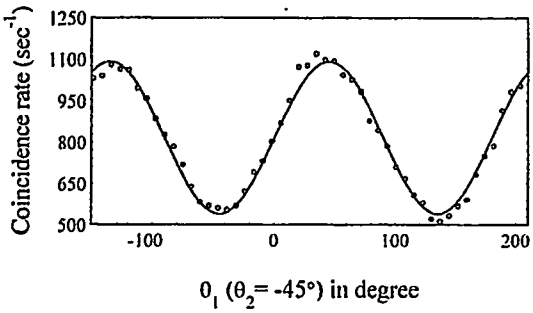

Figure 8 Measurement of the polarization entanglement. The polarization analyzer of photon *B* was varied, while that of photon *A* was fixed at –45°. The solid line is the fitting with $\sin^2(\theta_1 + \theta_2)$.

III. THEORETICAL CHALLENGES

The nonlocality of the correlations of two particles in quantum entanglement has no classical analog. It allows coherent effects to occur instantaneously in spatially separate locations. The question naturally arises as to whether a more general formulation of QT could provide a basis for superluminal communications. This issue has recently been the subject of considerable debate in the open literature.

There are basically two schools of thought: one, which precludes this possibility (based, for example, on conflicts with the theory of special relativity), and one which allows it under special provisions. We will discuss these issues in some detail in the sequel. First, however, we briefly highlight a few of the more significant new findings in the growing experimental and theoretical evidence of superluminal effects.

A conference on superluminal velocities took place in June 1998 in Cologne [21]. Theoretical and experimental contributions to this topic focused primarily on evanescent mode propagation and on superluminal quantum phenomena. The issues of causality, superluminality, and relativity were also examined. In the area of electromagnetic propagation, two exciting developments were addressed. Nimtz reported on experimental measurements of superluminal velocities achieved with frequency band-limited signals carried by evanescent modes [22]. Specifically, he timed a microwave pulse crossing an evanescent barrier (e.g., undersized waveguides, or periodic dielectric heterostructures) at $4.7c$. He demonstrated that, as consequence of the frequency band limitation of information signals, and if all mode components are evanescent, an actual signal might travel faster than the speed of light. Capelas de Oliveira and Rodrigues introduced the intriguing theory of superluminal electromagnetic X-waves (SEXW) defined as undistorted progressive waves solutions of the relativistic Maxwell equations [23]. They present simulations of finite aperture approximations to SEXW, illustrate the signaling mechanism, and discuss supporting experimental evidence.

What are the key arguments put forward against the possibility of superluminal signaling? Chiao and Steinberg analyze quantum tunneling experiments and tachyon-like excitations in laser media [24]. Even though they find the evidence conclusive that the tunneling process is superluminal, and that tachyon-like excitations in a population-inverted medium at frequencies close to resonance give rise to superluminal wave packets, they argue that such phenomena can not be used for superluminal information transfer. In their view, the group velocity can not be identified as the signal velocity of special relativity, a role they attribute solely to Sommerfeld's front velocity. In that context, Aharonov, Reznik, and Stern have shown that the unstable modes, which play an essential role in the superluminal group velocity of analytical wave packets, are strongly suppressed in the quantum limit as they become incompatible with unitary time evolution [25].

Let us now examine EPR-based superluminal schemes. Furuya *et al* analyze a paradigm proposed by Garuccio, in which one of the photons of a polarization-entangled EPR pair is incident upon a Michelson interferometer in which a phase-conjugation mirror (PCM) replaces one of the mirrors [26]. The sender (located at the source site) can superluminally communicate with a receiver (located at the detector site), based on the presence or absence of interferences at the detector. The scheme uses the PCM property that a reflected photon has the same polarization as the incident photon (contrary to reflection by an ordinary mirror), allowing to distinguish between circular and linear polarization. In a related context, Blaauboer *et al* also proposed [27] a connection between optical phase conjugation and superluminal behavior. Furuya *et al* prove that Garuccio's scheme would fail if non coherent light is used, because then the interferometer could not distinguish between unpolarized photons prepared by mixing linear polarization states or by mixing circular polarization states. They admit, however, that their counterproof would not apply to a generalized Garuccio approach, which would use coherent light states. Finally, in terms of criticism, let us mention the recent article by Peres [28], where criteria that prevent superluminal signaling are established. These criteria must be obeyed by various operators involved in classical interventions on quantum systems localized in mutually spacelike regions.

What are the arguments in favor of superluminal information transfer? Gisin shows [29] that Weinberg's general framework [30] for introducing nonlinear corrections into quantum mechanics allows for arbitrary fast communications. It is interesting to note that, in a recent book [31], Weinberg himself states: "I could not find a way to extend the nonlinear version of quantum mechanics to theories based on Einstein's special theory of relativity (...) both N. Gisin in Geneva and my colleague Joseph Polchinsky at the University of Texas independently pointed out that (...) the nonlinearities of the generalized theory *could* be used to send signals instantaneously over large distances".

At the Cologne symposium [21] Mittelstaedt reviewed the arguments that had been put forward in recent years in order to show that non-local effects in quantum systems with EPR-like correlations can not be used for superluminal communications. He demonstrated that most of these arguments are based on circular proofs. For instance, a "locality principle" can not be used to exclude superluminal quantum signals and to justify quantum causality, since the locality principle itself is justified by either quantum causality or an equivalent "covariance postulate" [32]. In a similar vein, van Enk shows that the proof given by Westmoreland and Schumacher in [33] that superluminal signaling violates the quantum no-cloning theorem is in fact incorrect [34]. Hegerfeld uses the formalism of relativistic quantum mechanics to show that the wave function of a free particle initially in a finite volume instantaneously spreads to infinity and, more importantly, that transition probabilities in widely separated systems may also become nonzero instantaneously [35]. His results hold under amazingly few assumptions (Hilbert space framework and positivity of the energy). Hegerfeld observes that, in order to retain Einstein causality, a mechanism such as "clouds of virtual particles or vacuum fluctuations" would be needed. To conclude this review, we note a recent suggestion of Mittelstaedt [36]. If the existence of superluminal signals is assumed *ab initio* (viz. [22] and [35]), and consequently a new space-time metric (different from the Minkowskian metric) is adopted, all the paradoxes and difficulties discussed above would immediately disappear.

IV. FUTURE ACTIVITIES

In this paper, we have presented recent progress achieved at CESAR/ORNL in the area of QT. We have also highlighted some of the formidable theoretical challenges that must be overcome if an application of this technology to communications is to become possible. The feasibility question is, in our minds, still open. To summarize, we now succinctly indicate our near-term proposed road map.

From a theory perspective, we will focus our attention on two recent proposals for superluminal communications. Greenberger has demonstrated [37] that if one can construct a macroscopic Schrodinger cat state (i.e., a state that maintains quantum coherence), then such a state can be used for sending superluminal signals. His scheme assumes that the following two requirements can be realized. First, it should be possible to entangle the signal-transmitting device with the signal itself, thereby constructing a GHZ state. Second, that non-unitary evolution can be established and controlled in a subset of the complete Hilbert space. This latter property has already been demonstrated successfully in several downconversion experiments. Greenberger uses an optical phase shifter as model for his signaling device. We believe that as of this date better alternatives are available. The second Gedankenexperiment we intend to examine was introduced by Srikanth [37]. His proposed method uses a momentum-entangled EPR source. Assuming a pure ensemble of entangled pairs, either position or momentum is measured at the sender. This leaves the counterpart in the EPR pair as either a localized particle or a plane wave. In Srikanth's scheme, the receiver distinguishes between these outcomes by means of interferometry. Since the collapse of the wavefunction is assumed to be instantaneous, superluminal signal transmission would be established.

We intend to explore possible experimental realizations of the above paradigms. We will also continue to focus on cascaded type-II OPDC, with emphasis on walk-off, optical collimation, optimal generation efficiency, and maximal entanglement. Special attention will also be given to multi-photon entanglement.

ACKNOWLEDGMENT

This research was performed at the Oak Ridge National Laboratory (ORNL), managed by UT-Battelle, LLC for the United Stated Department of Energy (U. S. DOE) under Contract No. DE-AC05-00OR22725. Funding for the effort was provided the Basic Energy Sciences Engineering Research Program of the Office of Science, U.S. DOE.

REFERENCES

1. Y. Aharonov and D. Albert, "Can we make sense of the measurement process in relativistic quantum mechanics?", *Phys. Rev.*, **D 24**(2), 359-370 (1981).
2. C. Bennett, G. Brassard, C. Crepeau, R. Jozsa, A. Peres and W. Wootters, "Teleporting an unknown quantum state via dual classical and Einstein-Podolsky-Rosen channels, " *Phys. Rev. Lett.*, **70**(13), 1895-1899 (1993).
3. A. Einstein, B. Podolsky and N. Rosen, "Can quantum mechanical description of physical reality be considered complete?, " *Phys. Rev.*, **47**, 777-780 (1935).
4. L. Vaidman, "Teleportation of quantum states", *Phys. Rev.*, **A 49**(2), 1473-1476 (1994).
5. S. Braunstein and J. Kimble, "Teleportation of continuous quantum variables", *Phys. Rev. Lett.*, **80**(4), 869-872 (1998).
6. S. Stenholm and P. Bardroff, "Teleportation of N – dimensional states", *Phys. Rev.*, **A 58**(6), 4373-4376 (1998).
7. S. Zubairy, "Quantum teleportation of a field state", *Phys. Rev.*, **A 58**(6), 4368-4372 (1998).
8. C. Maierle, D. Lidar, and R. Harris, "How to teleport superpositions of chiral amplitudes", *Phys. Rev. Lett.*, **81**(26), 869-872 (1998).
9. G. Brassard, S. Braunstein, and R. Cleve, "Teleportation as a quantum computation", *Physica D*, **120**, 43-47 (1998).
10. D. Bouwmeester, J. -W. Pan, K. Mattle, M. Eibl, H. Weinfurter, and A. Zeilinger, "Experimental quantum teleportation, " *Nature*, **390**, 575–579 (1997).
11. J.-W. Pan, D. Bouwmeester, H. Weinfurter, and A. Zeilinger, "Experimental entanglement swapping", *Phys. Rev. Lett.*, **80**(18), 3891-3894 (1998).
12. D. Boschi, S. Branca, F. De Martini, L. Hardy and S. Popescu, "Experimental realization of teleporting an unknown pure quantum state via dual classical and Einstein-Podolski-Rosen channels," *Phys. Rev. Lett.*, **80**(6). 1121-1125 (1998).
13. W. Tittel, J. Brendel, B. Gisin, T. Herzog, H. Zbinden, and N. Gisin, "Experimental demonstration of quantum correlations over more than 10 km", *Phys. Rev.*, **A 57**(5), 3229-3232 (1998).
14. W. Buttler, R. Hughes, P. Kwiat, S. Lamoreaux, G. Luther, G. Morgan, J. Nordholt, C. Peterson, and C. Simmons, "Practical free-space quantum key distribution over 1km", *Phys. Rev. Lett.*, **81**(15). 3283-3286 (1998).
15. M. Nielsen, E. Knill, and R. Laflamme, "Complete quantum teleportation using nuclear magnetic resonance", Nature, **396**, 52-55 (1998).
16. A. Furosawa, J. Sorensen, S. Braunstein, C. Fuchs, J. Kimble, and E. Polzik, "Unconditional quantum teleportation", *Science*, **282**, 706-710 (1998).
17. L. Vaidman and N. Yoran, "Methods for reliable teleportation", *Phys. Rev.*, **A 59**(1), 116-125 (1999).
18. L. Mandel and E. Wolf, *Optical Coherence and Quantum Optics*, Cambridge University Press (1995).
19. P. G. Kwiat, K. Mattle, H. Weinfurter, A. Zeilinger, A. V. Sergienko and Y. Shih, "New high-intensity source of polarization-entangled photon pairs," *Phys. Rev. Lett.*, **75**(24), 4337-4341 (1995).
20. P. G. Kwiat, E. Waks, A. G. White, I. Appelbaum and P. H. Eberhard, "Ultrabright source of polarization-entangled photons", *Phys. Rev. A.*, **60**(2), R773 –R776 (1999).
21. P. Mittelstaedt and G. Nimtz eds., " Workshop on Superluminal Velocities", Annalen *der Physik*, **7**(7-8), 591-592 (1998).
22. G. Nimtz, "Superluminal signal velocities", *Annalen der Physik*, **7**(7-8), 618-624 (1998).
23. E. C. de Oliveira and W. Rodriguez, "Superluminal electromagnetic waves in free space", *Annalen der Physik*, **7**(7-8), 654-659 (1998).
24. R. Chiao and A. Steinberg, "Quantum optical studies of tunneling and other superluminal phenomena", *Physica Scripta*, **T76**, 61-66 (1998).
25. Y. Aharonov, B. Reznik, and A. Stern, "Quantum limitations of superluminal propagation", *Phys. Rev. Lett.*, **81**(11). 2190-2193 (1998).
26. K. Furuya, P. Milonni, A. Steinberg, and M. Wolinsky, "Failure of a proposed superluminal scheme", *Phys. Lett.*, **A 251**, 294-296 (1999).
27. M. Blaauboer, A. Kozekhin, A. Kofman, G. Kurizki, D. Lenstra, and A. Loder, "Superluminal pulse transmission through a phase conjugating mirror", *Optics Communications*, **148**, 295-299 (1998).
28. A. Peres, "Classical intervention in quantum systems. II. Relativistic invariance", *Phys. Rev.*, **A 61**, 022117(8) (2000).
29. N. Gisin, "Weinberg's non-linear quantum mechanics and superluminal communications", *Phys. Lett.*, **A 143**, 1-2 (1990).
30. S. Weinberg, "Testing Quantum Mechanics", *Ann. Phys.*, **194**, 336-386 (1989).
31. S. Weinberg, *Dreams of a Final Theory*, pp. 88-89, Vintage Books (1992).
32. P. Mittelstaedt, "Can EPR-correlations be used for the transmission of superluminal signals?", *Annalen der Physik*, **7**(7-8), 710-715 (1998).
33. M. Westmoreland and B. Schumacher, "Quantum entanglement and the non existence of superluminal signals", arXiv: quant-*phys*/9801014, Los Alamos National Laboratory (March 1998).
34. S. van Enk, "No-cloning and superluminal signaling", *arXiv: quant-phys*/9803030, Los Alamos National Laboratory (March 1998).
35. G. Hegerfeldt, "Instantaneous spreading and Einstein causality in quantum theory", *Annalen der Physik*, **7**(7-8), 716-725 (1998).
36. P. Mittelstaedt, "What if there are superluminal signals?", *Eur. Phys. Jour.*, **B 13**, 353-355 (2000).
37. D. Greenberger, "If one could build a macroscopical Schrodinger cat state, one could communicate superluminally", *Physica Scripta*, **T76**, 57-60 (1998).
38. R. Srikanth, "Noncausal superluminal nonlocal signaling", *arXiv: quant-phys*/9904075, Los Alamos National Laboratory (July 1999).

ENZYME ADSORPTION AND FUNCTION AT INTERFACES

L.G. Cascão-Pereira, C.J. Radke and H.W. Blanch

Department of Chemical Engineering

University of California

Berkeley, CA USA

Thin-film forces between fluid interfaces with adsorbed protein are of pivotal importance for the stabilization of many foams and emulsions encountered in the dairy and pharmaceutical industry. We have developed a novel type of microfabricated film holder, which extends the thin-film balance (TFB) technique to the study of protein foam films. With this technique we can directly measure the forces responsible for stable film formation and investigate film drainage and coalescence. Force curves are presented for the first time for two proteins: β-casein and bovine serum albumin.

Stable protein films are obtained at pH close to the protein isoelectric point or away from it where all the charge is screened by addition of electrolyte. These films are stabilized mainly by steric repulsive forces leading to black films of the dimensions of a protein bilayer. Gray films stabilized by mainly electrostatic forces are only observed at extremely low forces. As a necessary condition for film stability, protein must readily adsorb at the interface, which correlates with a significant reduction in surface tension. Film history is shown to strongly influence thin-film stability and drainage.

THIN-FILM FORCES

We have extended the thin-film balance technique (TFB) to the study of protein films under varying conditions of concentration, ionic strength, pH, and degree of aging at the interface. A novel film holder has been designed to investigate small protein and enzyme samples under equilibrium and dynamic conditions. With this technique we can study the rates of drainage of thin films and examine the forces that dictate their stability. The behavior of single thin films is representative of the observed macroscopic behavior of foams and emulsions.

When the distance of separation between two fluid-fluid interfaces in a foam or emulsion is below 100 nm, the effects of van der Waals attraction and electrostatic repulsion become important. At distances of separation below a few nanometers repulsive steric and structural forces become important. The combined effects of these forces are expressed through the disjoining pressure $\Pi(h)$, which is the net sum of forces per unit area acting normal to the interfaces as a function of their separation h. Moreover, the disjoining pressure is the negative derivative of the potential of mean force or interaction potential W, per unit area, with respect to film thickness h [1-3].

$$\Pi = -\frac{\partial W}{\partial h} \qquad (1)$$

Thin-film stability is achieved when the disjoining pressure is repulsive, the film then resists thinning and rupture due to small perturbations. Because proteins adsorb at interfaces, they affect thin-film stability through their contribution to the disjoining pressure Π(h). At equilibrium and in the flat portion of the film, the disjoining pressure Π is equal to the imposed capillary pressure P_C. The latter, is simply the difference between the gas pressure, P_G, and the bulk liquid pressure, P_L, in the Plateau border region surrounding the film:

$$P_C \equiv P_G - P_L = \Pi \tag{2}$$

It is customary to separate the various contributions to the disjoining pressure into different components as in Figure 1:

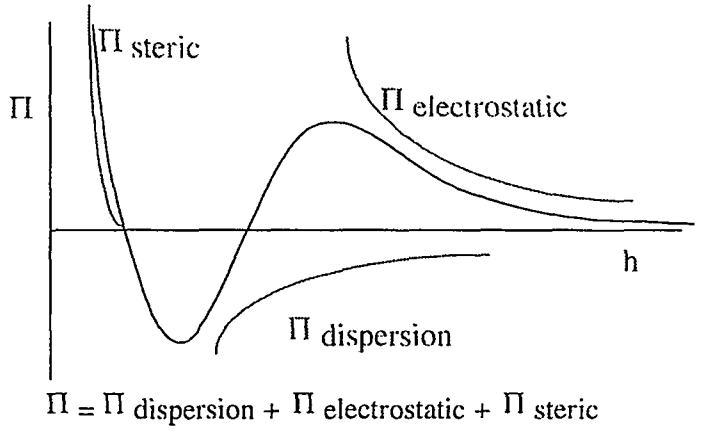

Figure 1. Idealized Disjoining Pressure Isotherm.

The well-known DLVO theory accounts for the dispersion and electrostatic components of Π as respectively expressed below:

$$\Pi(h) = -\frac{A_{12}}{6\pi h^3} + 64 n^0 kT\gamma^2 \exp(-\kappa h)$$
$$\gamma = \frac{\exp(Z/2)-1}{\exp(Z/2)+1}, \quad Z = \frac{e\psi_0}{kT} \tag{3}$$

where A_{12} is known as the Hamaker constant. n^0 is the number density of ions in the bulk solution, k is the Boltzmann constant, T is the temperature, κ is the inverse Debye length, e is the electron charge and ψ_0 is the potential. The weak-overlap approximation is used here for the electrostatic contribution. The simplest way to account for steric repulsion at small separations is to assume a hard-sphere potential. Details can be found elsewhere [6]. Scheludko and Vrij use thermodynamic and fluid-mechanical analyses to establish that thin-films can not exist at thicknesses for which $\partial\Pi/\partial h > 0$ [4,5]. Accordingly, only thickness branches along which $\partial\Pi/\partial h < 0$ are accessible through experiment.

THIN-FILM BALANCE

Disjoining pressure isotherms can be measured using a device now called a thin-film balance [7-11]. This device operates by maintaining a balance between capillary and thin-film forces. Thin films are formed in a film holder fused to a capillary tube, which is enclosed in a hermetically sealed cell with the capillary tube exposed to a constant external reference pressure.

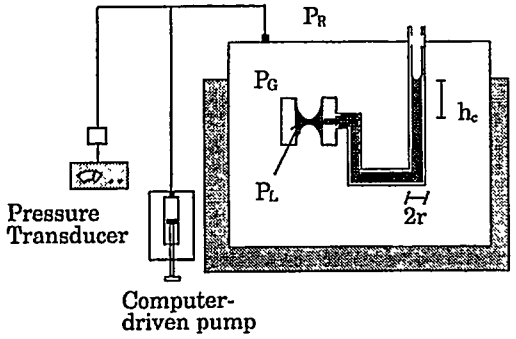

Figure 2. Schematic of Conventional Film Holder and Cell.

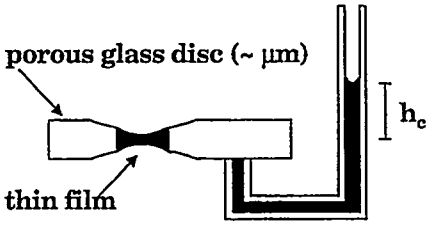

Figure 3. Schematics of a Porous-Plate Cell.

The cell is mounted on a pneumatic vibration isolation table and can be thermostated if desired. The gas pressure in the cell is regulated with both a manual and a computer-driven syringe pump. Manipulation of the cell pressure alters the imposed pressure on the film (i.e. the capillary pressure) and thus, sets the disjoining pressure. Film thicknesses are measured interferometrically, within ± 0.5 nm, using the method of Scheludko and Platikanov [10]. The experimental setup is summarized in Figure 4.

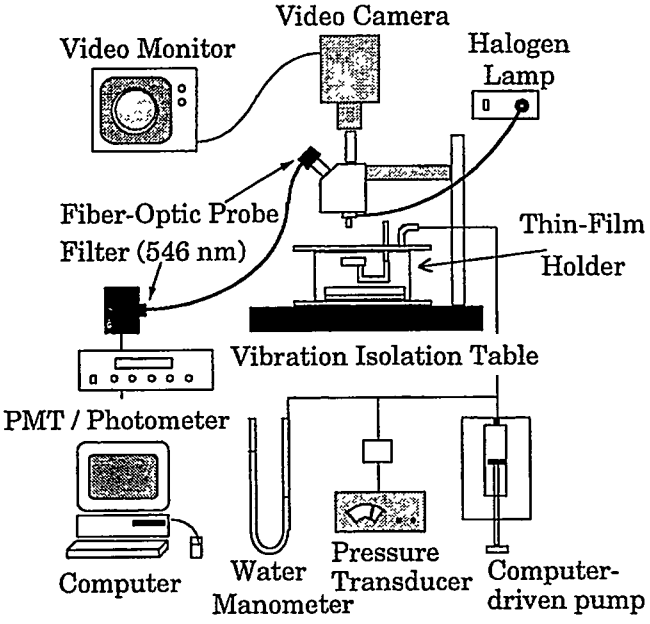

Figure 4. Schematic of a Thin-Film Balance.

We developed a unique microfabricated film holder suitable for the study of protein solutions based on a previous design by Velev *et al* [12]. This new design combines the advantages of both types of film holders currently used for the investigation of surfactant solutions. It is referred throughout the rest of this paper as the bike-wheel microcell, for reasons that will become apparent shortly. The principle of operation of the bike-wheel microcell is similar to that of the capillary type. However, due to the modified design the dimensions of the capillary into which the film is formed are reduced 10-fold, whereas the dimensions of the pores through which solution drains are reduced 100-fold. The capillary pressures attained are comparable to those obtained with the porous-plate technique and film dimensions

are closer to those encountered in real foams and emulsions [13,14]. Due to the miniaturization of the whole structure, the drainage time necessary to observe thin plane-parallel films is drastically reduced allowing the investigation of force laws as a function of time. Moreover, the surface area in contact with protein solution is also decreased, rendering the loss of protein due to adsorption on the glass walls negligible and allowing the investigation of systems for which only small amounts are available.

A micrograph of the bike-wheel microcell is shown in Figure 5.

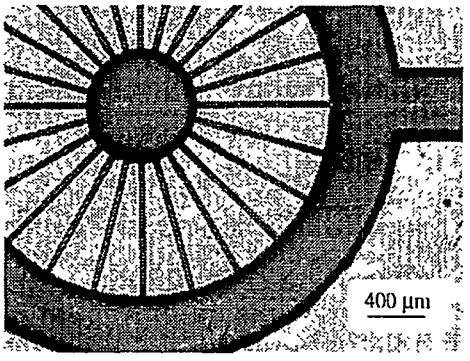

Figure 5. Portion of Microcell Upper Plate Magnified Under a Microscope.

RESULTS AND DISCUSSION

β-casein

The next series of experiments deals with β-casein a naturally occurring dairy protein used industrially as a stabilizing agent in many foams and emulsions. β-casein from bovine milk is a flexible, loosely structured protein without disulfide bonds, of molecular weight 24 kDa, pI 5.2 and a radius of gyration of 46 Å [15-17].

The effect of protein concentration is presented for β-casein aqueous solutions with no added electrolyte. The results are summarized in Figure 6. A black thin film is observed at 0.05 wt.% β-casein solutions. These films are stable over several orders of magnitude of the disjoining pressure. At 0.1 wt.% only gray thicker films are observed for the disjoining pressure range investigated. At the intermediate concentration of 0.075 wt.% a thickness transition from gray (outer branch) to black (inner branch) films occurs. Therefore, as the protein concentration is increased, the formation of thicker films and appearance of an outer branch becomes possible.

The observed 18-nm thick black films are consistent with the picture of a β–casein bilayer stabilized by purely steric repulsive forces. Gray films are stabilized by long range repulsive forces, albeit low in magnitude. The nature of these forces is less clear. As the protein concentration is increased the

outer branch becomes sharper, thus suggesting an electrostatic effect associated with the protein charge, even if low at this pH since we are close to the isoelectric point.

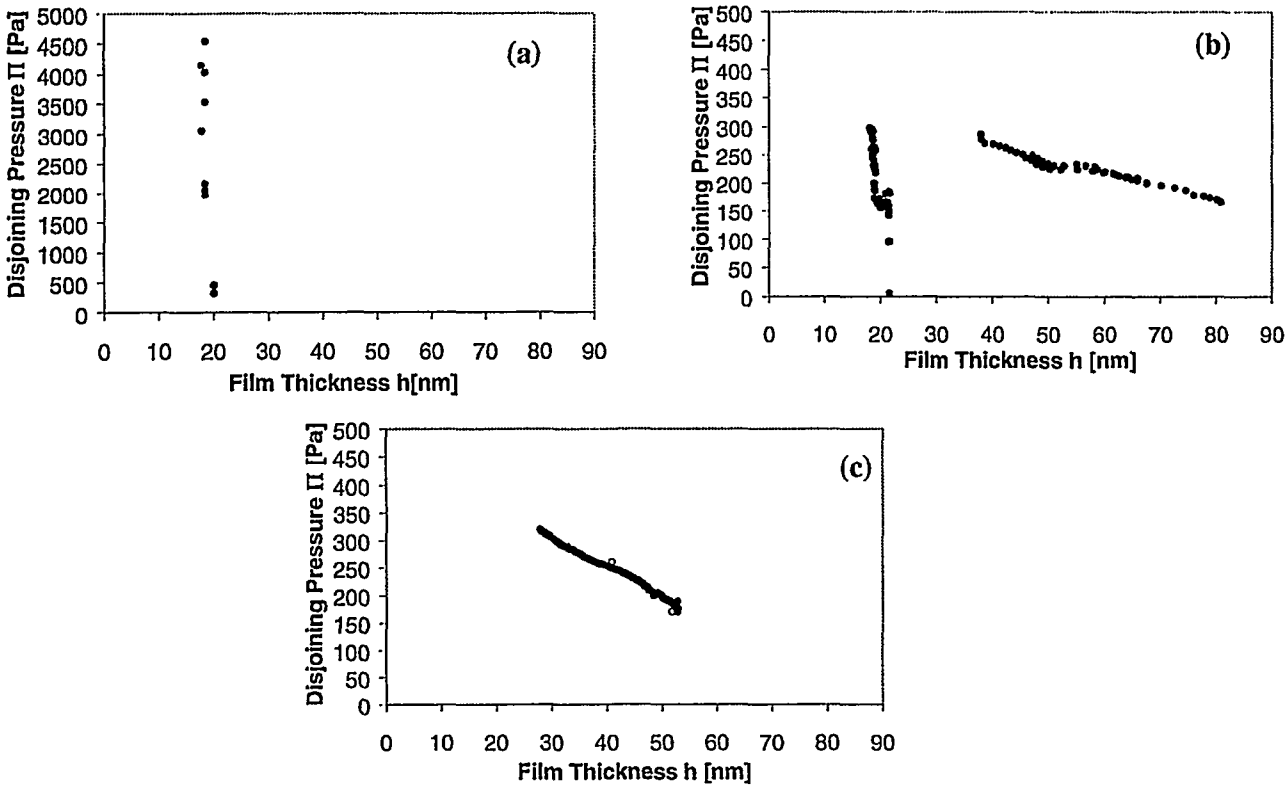

Figure 6 - The Effect of β-Casein Concentration on the Disjoining Pressure Isotherm.

Disjoining pressure isotherms are presented in Figure 7 for 0.1wt.% β-casein aqueous solutions with NaCl as the added electrolyte. Data obtained dynamically is in close agreement with equilibrium values. Solutions with 100 mM NaCl exhibit only one branch, 25-nm thick. Differences in the observed isotherms at this electrolyte concentration may arise from differences in solution preparations. Solutions with 10 mM NaCl exhibit a thickness transition from a 28-nm gray film to an 18-nm black film. The thickness of the inner branch is the same as previously observed for β-casein solutions at low concentrations and no added electrolyte (Figure 6(a) and (b) inner branch). With no added electrolyte, only thick gray films are observed as in Figure 6(c).

These findings are consistent with the picture of an inner branch stabilized by steric forces due to the excluded volume of the proteins and an outer branch stabilized by electrostatic double-layer forces. Indeed, as the electrolyte concentration increases the outer branch becomes sharper due to the ionic screening of the protein charges by the electrolyte. Eventually, a thickness transition arises as with 10 mM NaCl solutions. This thickness transition is consistent with the squeezing out of one protein diameter. When the electrolyte concentration is further increased, no transition is observed and films are 25-nm thick.

Comparison of Figure 7(b) and Figure 8 provides further evidence that electrostatic forces stabilize thicker, gray films. As the solution pH is increased from 5.8 to 9.0, keeping all other parameters the same, the outer branch becomes less sharp probably due to the increased repulsion between charged protein molecules.

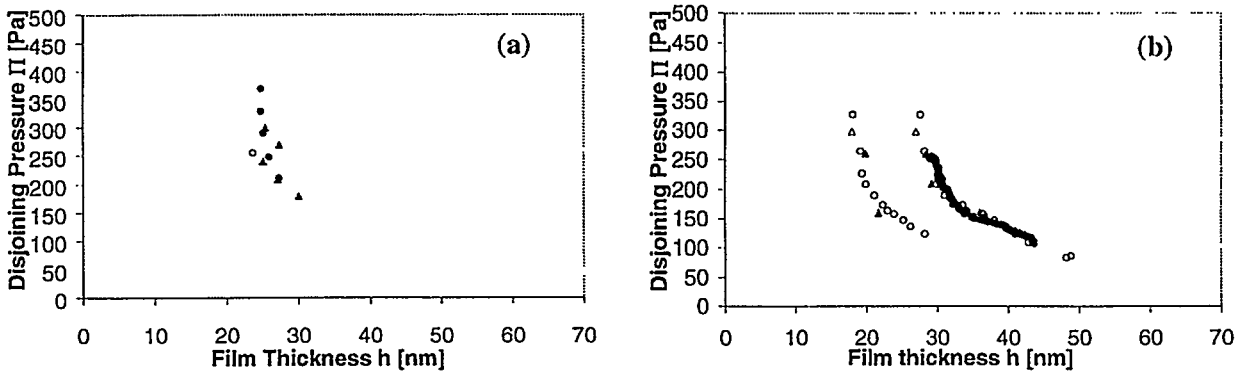

Figure 7- Effect of electrolyte concentration on the disjoining pressure isotherms of β-casein.

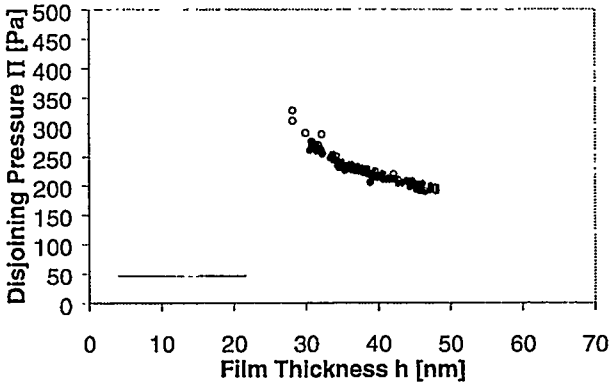

Figure 8 - Disjoining pressure isotherm for a solution of 0.1 wt.% β-casein with 10 mM NaCl, pH 9.0.

Bovine Serum Albumin

We decide to contrast the observed film behavior of β-casein with that of bovine serum albumin, a model globular protein. In opposition to the flexible, loosely structured β-casein, BSA is a large, rigid, globular protein, of approximate dimensions 60 Å in aqueous solution, molecular weight 66.5 kDa, pI 4.7 and 17 disulfide bonds. The primary function of this protein is regulation of the colloidal osmotic pressure of blood [17].

The disjoining pressure isotherms for 0.1 wt% BSA at pH 5.2 under different electrolyte concentrations are shown in Figure 9. The overall force measured is low, similar to β-casein films. At about 500 Pa there is film rupture. Only one branch is observed. The isotherm at 0.1 mM or 1.0 mM NaCl fall on top of each other. At this pH, close to the isolectric point there is very little charge on the protein. This net charge is most likely all screened by the available electrolyte in both cases. The final film thickness is close to 12 nm (± 1 nm given the scatter in the data for these runs) which is about twice the size of a BSA molecule in solution, thus suggesting a bilayer with no bulk solution in between stabilized by steric repulsive forces alone due to the excluded volume of the proteins.

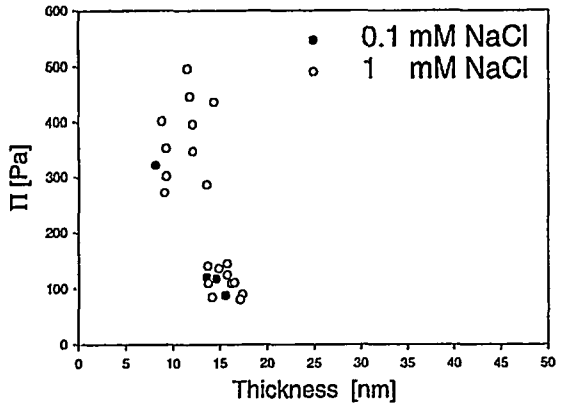

Figure 9 – Effect of electrolyte addition on the disjoining pressure isotherm of BSA at pH 5.2.

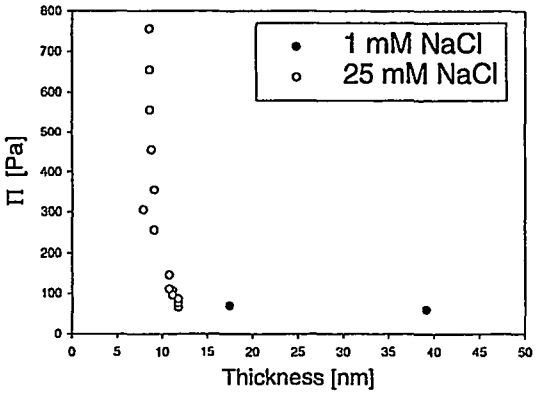

Figure 10 – Effect of electrolyte addition on the disjoining pressure isotherm of BSA at pH 8.3.

At pH away from the isoelectric point, such as 8.3 where there is a net negative charge on the protein, the picture is very different as shown in Figure 10. As a matter of fact no stable films are formed with 0.1 mM NaCl. With 1 mM NaCl a 40-nm thick protein film is formed at extremely low pressures such as 50 Pa. Upon an increase in pressure up to 60 Pa already a transition is observed until a 18-nm thin film is obtained. Upon further increases in pressure the film will rupture. Stable films are obtained at this pH upon addition of 25 mM NaCl. All the charge on the protein is screened and a black, thin film is immediately obtained. The film obtained is about 8-nm thick, just slightly bigger than the dimension of BSA in solution thus suggesting that a monolayer of protein bridging in between both film interfaces may be enough to stabilize this film.

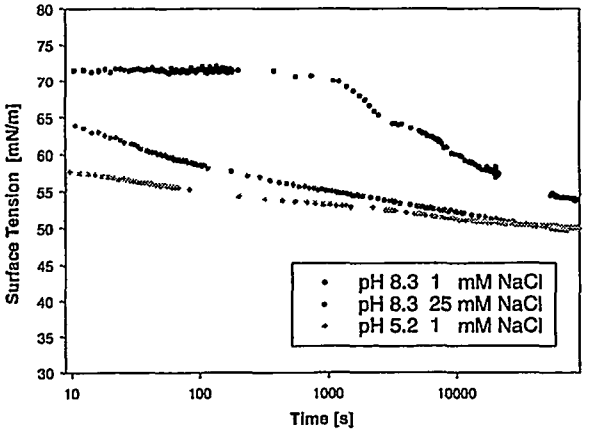

Figure 11 – Dynamic surface tensions for 0.1 wt% BSA under different pH and ionic strengths.

Dynamic tension measurements for the solutions discussed above are extremely useful for complementing our understanding of the overall stability mechanism. In Figure 11 we notice that at pH 5.2, 1mM NaCl and pH 8.3, 25 mM NaCl the measured tension quickly decreases from the value of the pure air/water interface 72 mM/m to values close to 55 mN/m. On the other hand, at pH 8.3 and only 1 mM NaCl when the protein is charged and there is not enough electrolytes present to screen these charges, the measured tension value remains close to 72 mM/m for considerably longer times. There is a significant electrostatic barrier for adsorption at high charges indicating little adsorption of protein molecules for extended times.

Stable films of proteins are obtained at pH close to the isoelectric point or at pH away from the isoelectric point with enough electrolyte to screen the net charges present on the molecule. Under these conditions protein is able to adsorb at the air/water interface as indicated by a significant lowering in surface tension. Steric repulsive forces stabilize the films obtained.

THICKNESS TRANSITION MECHANISM AND RATES OF DRAINAGE AND COALESCENCE

Our studies indicate that thin-film stability and rates of drainage and coalescence are highly dependent on film history.

Figure 12 below shows the case of a fresh BSA protein film, i.e. the protein was allowed to adsorb at the interface for 30 minutes prior to measurement, undergoing a first-order thickness transition at a constant applied pressure.

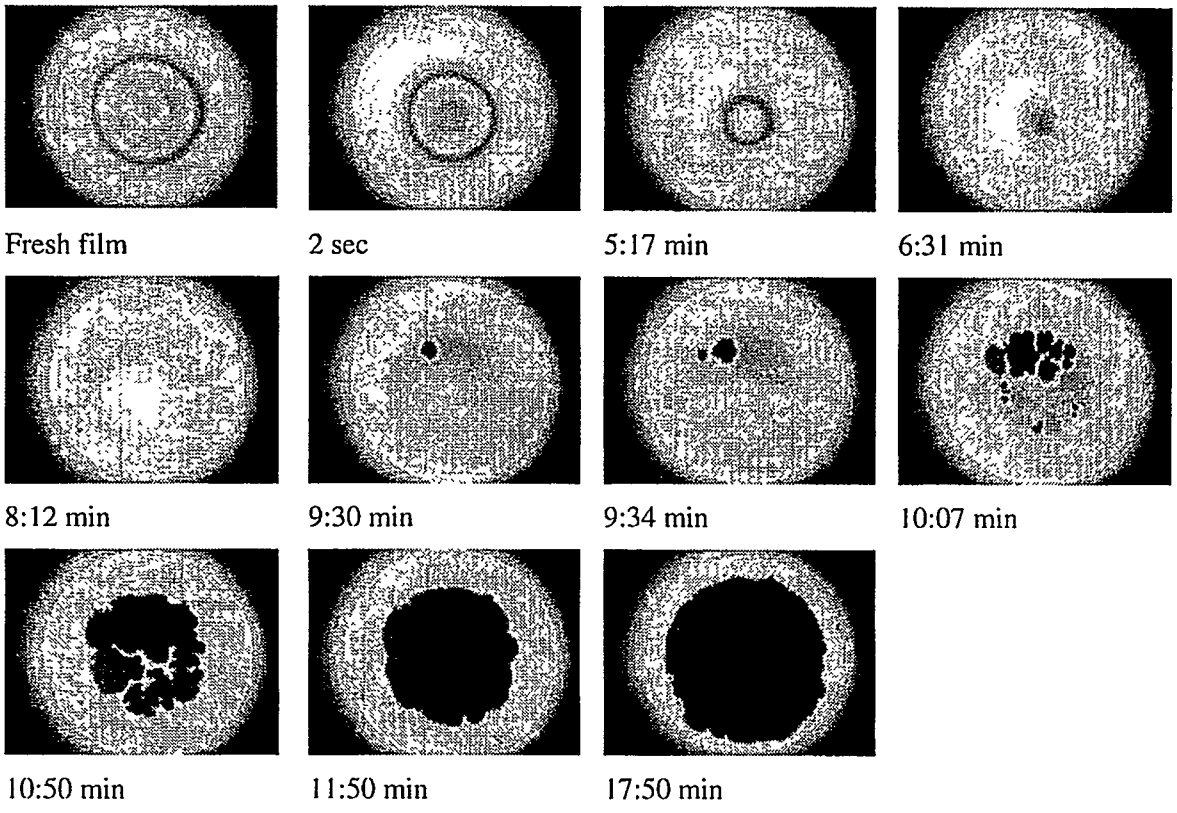

Figure 12 – Initial formation and thickness transition of a 0.01 wt% BSA fresh film at pH 5.2, 1 mM NaCl.

The features discussed hereafter are typical of protein films, β-casein having a similar behavior. Upon bringing the two menisci from a thick biconcave lens into contact, the film is formed as indicated by the characteristic circular Newton interference rings. This film is initially very thick (hundreds of nanometers), with a dimple in the center, and it will drain after about 8 min to a homogeneous equilibrium flat film of constant thickness throughout. At about 9:30 min a thickness transition from a yellow, gray about 40-nm thick film to a more stable thin, black film takes place. Black spots appear close to the center and grow by fingering until eventually (after another hour) the entire film interface is that of a black film 15-nm thick.

The drainage and transition mechanism of a protein film is completely different than that of low molecular weight surfactants. Contrary to surfactant films, the dimple thins in place. Moreover, small particles present at the film interface remain in relative position while thinning. The thickness transition happens through a fingering mechanism with non-equilibrium lines of tension. The overall rate of drainage is much greater, on the order of minutes to hours rather than seconds. These are features characteristic of immobile interfaces most likely due to gelation at the level of the interface through protein entanglement already at very early times. This black film is stable over hundreds of Pascal and will resist upon further increases in pressure.

One must consider films formed from protein solutions that had been at the interface for several hours. The film in Figure 13 is highly heterogeneous and does not drain to a flat film. It presents large protein agglomerates surrounded by regions of black films. This pattern remains under contraction and/or relaxation of the interface. When subject to large disturbances such as a capillary pressure increase, aged films will not thin further without breakage. Upon film reformation chunks of protein agglomerates are observed. Aged films seem to be brittle and have solid-like behavior. Other than aging at the interface, this type of film is also favored at high protein concentrations, solution pH value close to the isoelectric point, and at high electrolyte concentrations that decrease the electrostatic screening.

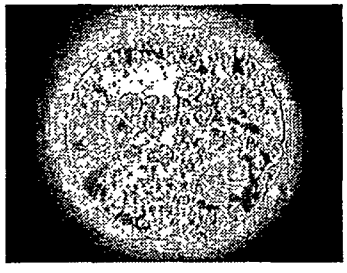

Figure 13 - Film formation from BSA 0.01 wt% pH 5.2 aged at the interface for several hours.

REFERENCES

1.) Derjaguin, B. V., and L. Landau, "Theory of the Stability of Strongly Charged Lyophobic Salts and of the Adhesion of Strongly Charged Particles in Solutions of Electrolytes," *Acta Physicochimica URSS*, **14** pp.633-663 (1941)

2.) Verwey, E. J. W., and J. T. G. Overbeek, Theory of the Stability of Lyophobic Colloids, Elsevier, Amsterdam (1948)

3.) Derjaguin, B. V., and E. Obuchov, "Anomalien dünner Flüssigkeitsschichten III," *Acta Physica URSS*, **5**(1) pp.1-22 (1936)

4.) Scheludko, A., "Sur certaines particularités des lames mousseuses: II. Stabilité cinétique, épaisseur critique et épaisseur d'équilibre," *Nederlandse Akademie van Wetenschappen - Proceedings B - Physical Sciences*, **B65** pp.87-96 (1962)

5.) Vrij, A., "Possible Mechanism for the Spontaneous Rupture of Thin, Free Liquid Films," *Discussions of the Faraday Society*, **42** pp.23-33 (1966)

6.) Israelachvili, J., Intermolecular & Surface Forces, (2nd Ed.) Academic Press, (1992)

7.) Scheludko, A., "Über das Ausfliessen der Lösung aus Schaumfilmen," *Kolloid-Zeitschrift*, **155**(1) pp.39-44 (1957)

8.) Scheludko, A., "Thin Liquid Films," *Advances in Colloid and Interfacial Science*, **1** pp.391 (1967)

9.) Bergeron, V., and C. J. Radke, "Equilibrium Measurements of Oscillatory Disjoining Pressures in Aqueous Foam Films," *Langmuir*, **8** pp.3020-3026 (1992)

10.) Scheludko, A., and D. Platikanov, "Untersuchung dünner flüssiger Schichten auf Quecksilber," *Kolloid-Zeitschrift*, **175** (1960)

11.) Scheludko, A., and D. Exerowa, "Über den elektrostatischen und van der Waalsschen zusätzlichen Druck in wässerigen Schaumfilmen," *Kolloid Zeitschrift*, **168**(1) pp.24-28 (1959)

12.) Velev, O. D., G. N. Constantinides, D. G. Avraam, A. C. Payatakes, et al., "Investigation of Thin Liquid Films of Small Diameters and High Capillary Pressures by a Miniaturized Cell," *Journal Of Colloid and Interface Science*, **175**(1) pp.68-76 (1995)

13.) Dalgleish, D. G., D. S. Horne, and A. J. R. Law, "Size-Related Differences In Bovine Casein Micelles," *Acta Biochimica Et Biophysica*, **991**(3) pp.383-387 (1989)

14.) Singh, G., C. A. Miller, and G. J. Hirasaki, "On dimple formation in foam films," *Journal Of Colloid and Interface Science*, **187**(2) pp.334-337 (1997)

15.) Leaver, J., and D. G. Dalgleish, "The Topography of Bovine Beta-Casein at an Oil Water Interface as Determined from the Kinetics of Trypsin-Catalysed Hydrolysis," *Acta Biochimica Et Biophysica*, **1041**(3) pp.217-222 (1990)

16.) Dickinson, E., D. S. Horne, J. S. Phipps, and R. M. Richardson, "A Neutron Reflectivity Study of the Adsorption of b-Casein at Fluid Interfaces," *Langmuir*, **9** pp.242-248 (1993)

17.) Atkinson, P. J., E. Dickinson, D. S. Horne, and R. M. Richardson, "Neutron Reflectivity of Adsorbed beta-casein and beta-lactoglobulin at the Air/Water Interface," *Journal of the Chemistry Society Faraday Transactions*, **91** pp.2847-2854 (1995)

METABOLIC ENGINEERING OF BIODEGRADABLE PLASTIC PRODUCTION BY CYANOBACTERIA: MODEL STUDIES IN *Synechocystis* sp. PCC6803

Gaspar Taroncher-Oldenburg and Gregory Stephanopoulos

Chemical Engineering Dept., Massachusetts Institute of Technology
Cambridge, Massachusetts 02139, U.S.A.

ABSTRACT

The accumulation of poly-3-hydroxyalkanoates (PHAs) by cyanobacteria has been proposed as a plausible process for the sequestration of atmospheric CO_2 and concomitant production of biodegradable plastic-like polymers. The application of metabolic engineering approaches to the analysis of PHA biosynthesis in cyanobacteria is illustrated here for the model organism *Synechocystis* sp. PCC6803.

INTRODUCTION

Over the past decade the need for a reduction of green house gases in the atmosphere has become an area of high priority in global warming research [1]. In particular, the development and implementation of technologies for the reduction and stabilization of CO_2 emissions through biotic carbon sequestration has been proposed [2]. One such application involves the accumulation of carbon-rich compounds by bacteria [3]. Several prokaryotes produce lipid storage materials called poly-3-hydroxyalkanoates (PHAs) that exhibit properties ranging from thermoplastic to elastomeric and are completely biodegradable [4].

The coupling of biosynthetic pathways leading to the production of PHAs with the ability of photoautotrophic organisms to provide the necessary precursors from CO_2 assimilated through photosynthesis, has been recognized as a promising approach to the efficient sequestration of atmospheric carbon dioxide (Fig. 1) [5]. In addition, the potential of commercializing these materials as plastic substitutes makes this application attractive from a commercial point of view [3].

This contribution explores some of the biological aspects of the application of metabolic engineering to the production of PHAs in a group of photoautotrophic prokaryotes, the cyanobacteria. Recent advances in the genetics and physiology of PHA production in the model organism *Synechocystis* sp. PCC6803 are presented, as well as some of the more practical issues related to the implementation of this technology are also discussed.

POTENTIAL FOR CO_2 UPTAKE BY CYANOBACTERIA

Cyanobacteria, a group of autotrophic photosynthetic organisms, have been proposed for implementing biological carbon sequestration systems [6]. Cyanobacteria exhibit significantly higher growth rates and CO_2 fixation efficiencies than higher plants [7]. The resulting high output per unit of biomass is further possible because of their high surface to volume ratio, the existence of specialized intracellular CO_2 concentrating mechanisms and the lack of any major supporting structures [8]. Cyanobacteria are currently being studied for production of the biofuels hydrogen and ethanol [9] and protein for the food industry and other technological applications [10].

Some of the factors still preventing the large scale application of cyanobacteria for the production of other commodity chemicals are, (a) the relatively slower growth rates of cyanobacteria and concomitant lower productivity, as compared to heterotrophic bacteria, such as *Escherichia coli*, (b) the inefficient transformation of light energy into biomass and metabolic products due to phenomena such as self-shading and sub-optimal photosynthetic turn-over rates, and (c) the energetic costs of downstream processing that can nullify any gain obtained from the fixation of CO_2 [6]. Efforts to overcome these limitations include the development of cyanobacterial strains with optimized product to biomass ratios [11], the design of photobioreactors that control turbulence to optimize gas exchange and light exposure for the organisms [12] and the over expression of product biosynthetic pathways as means of enhancing productivity and CO_2 fixation rates [13].

GENETIC ENGINEERING AND CYANOBACTERIA

Genetic analysis and manipulation of a handful of cyanobacteria has been successfully implemented over the last two decades [14]. *Synechocystis* sp. has been used as a model organism for photosynthesis research in the past, taking advantage of its capability for natural transformation [15]. We have recently described a PCR based transformation method that will facilitate the targeted insertion or deletion of specific genes in *Synechocystis* sp. [16]. The recent application of *Synechocystis* for the improved production of zeaxanthin and other carotenoids used as coloring agents for food, pharmaceuticals, cosmetics and animal feed, further shows the potential of this species to be used as a "photosynthetic factory" for the manufacture of specialty and commodity chemicals [13].

Genetic transformation of cyanobacteria with the PHA biosynthesis genes from *Alcaligenes eutrophus* [17] has been successfully attempted, and PHA accumulations between 1% and 17% Cell Dry Weight (CDW) have been reported [18,19]. With the characterization of the PHA biosynthetic pathway in *Synechocystis* sp. new possibilities are now at hand to genetically manipulate this pathway in cyanobacteria.

Finally, an important factor increasing the potential of applying genetic engineering approaches to cyanobacteria is the completion, or near completion of the genome sequencing of several species of cyanobacteria, including unicellular ones (e.g., *Synechocystis* sp.) and filamentous, diazotrophic representatives of this group (e.g., *Anabaena* sp.).

CYANOBACTERIA AND PHA PRODUCTION

The presence of PHA inclusion bodies in cyanobacteria was first reported by Carr in 1966, following the extraction of PHB from *Chloroglea fritschii* [20]. Since then, the occurrence of PHAs has been shown for several other species of cyanobacteria [21]. The most common type of PHA synthesized by cyanobacteria is poly-3-hydroxybutyrate (PHB) and, in some cases, also the more flexible poly(3-hydroxyvalerate) (P(3HV)) or the copolymer P(3HB-*co*-3HV) (Fig. 1; [21]). The biosynthesis of PHAs from acyl-CoA precursors takes place via three steps, as exemplified in Figure 1 for the case of PHB. The first reaction consists of the Claisen-type condensation of two molecules of acetyl-CoA to form

acetoacetyl-CoA. This step is catalyzed by a β-ketothiolase (acetoacetyl-CoA thiolase; EC 2.3.1.9). Acetoacetyl-CoA is then reduced by an acetoacetyl-CoA reductase (EC 1.1.1.36) to yield D(-)-3-hydroxybutyryl-CoA, followed by the polymerization reaction catalyzed by a PHA synthase (no EC number).

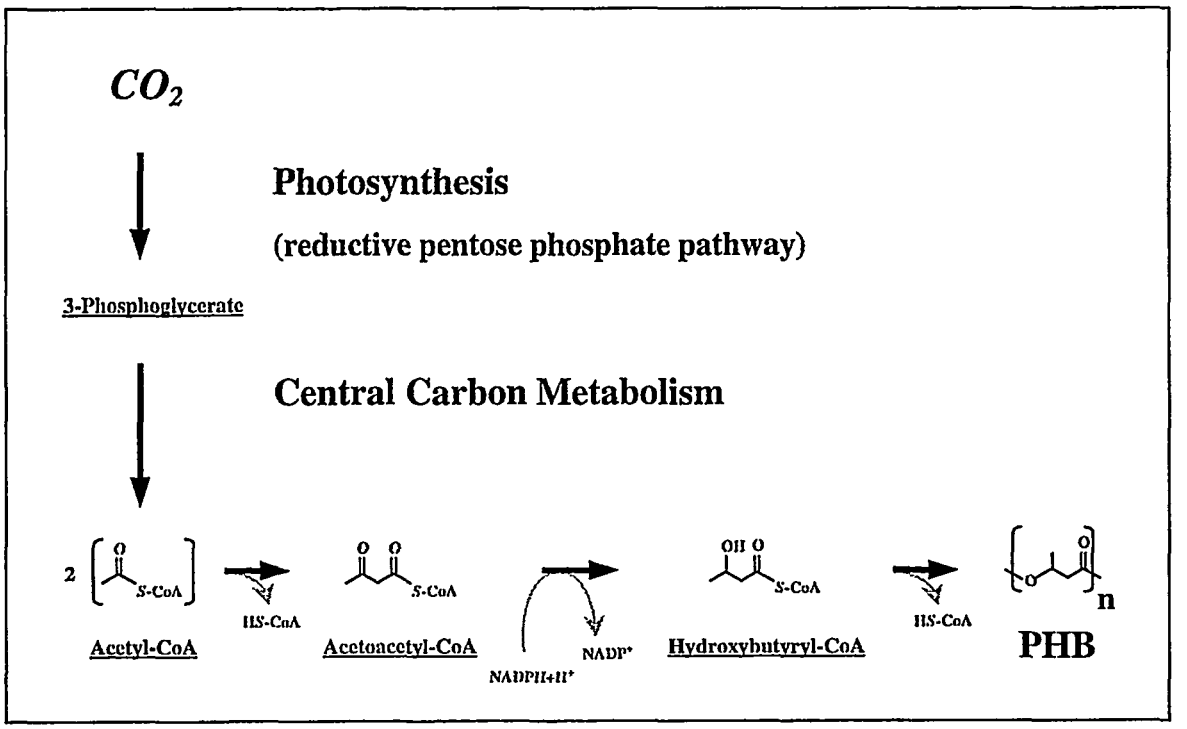

Figure 1. Diagram Showing the Coupling of Photosynthetic Carbon Dioxide Fixation and PHA production as exemplified for the case of poly-3-hydroxybutyrate (PHB).

Recently, and as a result of the availability of the full genome sequence of the cyanobacterium *Synechocystis* sp. PCC6803 [22], the first complete set of genes coding for the three enzymes involved in PHA synthesis in cyanobacteria has been identified and characterized [23,24] (Fig. 2).

The two subunits, $phaE_{Syn}$ and $phaC_{Syn}$, of the type III, two-component PHA synthase are encoded by two open reading frames (ORFs), $phaE_{Syn}$ (slr1829) and $phaC_{Syn}$ (slr1830) respectively, that are located contiguously and in the same orientation on the Synechocystis sp. PCC6803 chromosome (The gene classification and nomenclature used throughout this text is in accordance with the *Synechocystis* sp. PCC6803 genome project ([http://www.kazusa.or.jp/cyano/]; [22]) (subscripts to the genes refer to the species to which they belong [25]). Type III PHA synthases are characterized by their specificity for short-chain-length hydroxyalkanoic acids (three to five carbon atoms) and the existence of two subunits conforming the active dimer [25,26]. The PHA synthase activity of the two ORFs, slr1829 and slr1830, has been demonstrated by heterologous expression in *Escherichia coli* [23] , phenotypic complementation of a PHA-negative mutant of *Alcaligenes eutrophus* [23] and targeted deletion in *Synechocystis* sp. [16] . Only three other type III PHA synthases have been characterized to date (*Allochromatium* (*Chromatium*) *vinosum* [27], *Thiocystis violacea* [28] and *Thiocapsa pfennigii* [29]). In all three cases the other two biosynthetic genes, *phaA* and *phaB*, are clustered with the *phaE-phaC* genes. The primary annotation of the *Synechocystis* genome failed to identify any candidates for *phaA* or *phaB* in the vicinity of the ORF cluster slr1829-slr1830. A directed similarity search of the entire genome of this organism resulted in the identification of two strong candidate ORFs, slr1993 and slr1994, for the two genes in question, $phaA_{Syn}$

and $phaB_{Syn}$ respectively. Heterologous expression of the two genes together with the PHA synthase genes of *Synechocystis*, $phaE_{Syn}$ and $phaC_{Syn}$, resulted in PHA biosynthesis in *E. coli*. On the other hand, targeted gene disruption of $phaA_{Syn}$ and $phaB_{Syn}$ in *Synechocystis* caused the loss of PHA producing capacity of the organism [24].

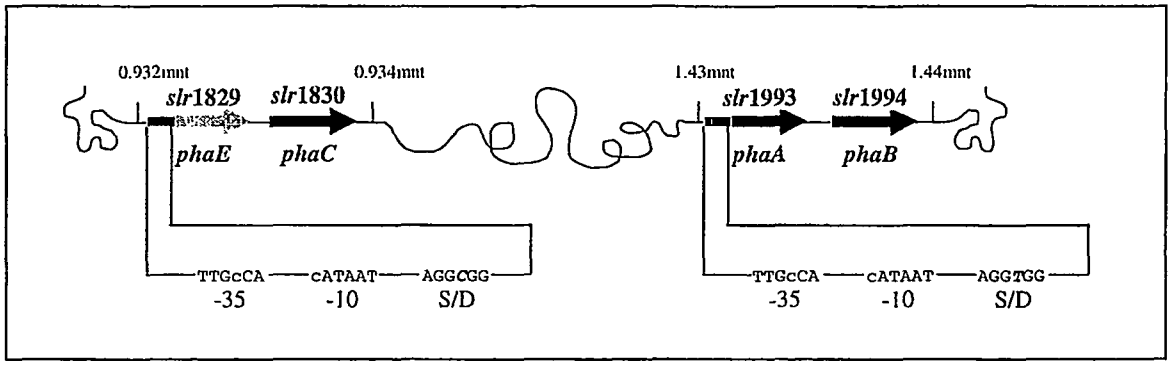

Figure 2. Structure and organization of the four anabolic *pha* genes in *Synechocystis* sp. PCC6803. Locations on the genome (in mnt) were determined from CyanoBase [http://www.kazusa.or.jp/cyano/]; hashed bars represent putative promoter regions; bold, cursive letters highlight the only difference between the two promoter regions; -35, -10 and S/D refer to the -35, -10 and Shine-Dalgarno consensus regions of σ^{70} in *E. coli* respectively; lower-case "c" indicates a discrepancy with the σ^{70} consensus region ("c" instead of "A" (-35); "c" instead of "T" (-10)).

REGULATION OF PHA PRODUCTION IN *Synechocystis* SP. PCC6803

PHAs fulfill several roles in the physiological balance of prokaryotic cells: They serve as a carbon reservoir, energy storage, or a combination of both in most heterotrophic bacteria [4], or as an electron acceptor or "fermentation product" during glycolysis, as has been proposed in the case of sulfur reducing bacteria such as *Chromatium vinosum*, or during acetate uptake by activated sludge in the anaerobic phase of the Enhanced Biological Phosphorus Removal (EBPR) process [30,31]. Two aspects of carbon metabolism are unique to cyanobacteria. First, all cyanobacteria accumulate the glucose-polymer glycogen as a carbon and energy reservoir [32]. Glycogen is oxidized via the pentose phosphate pathway and ATP is generated by aerobic respiration [32]. Secondly, the tricarboxylic acid cycle (TCA cycle) is interrupted in cyanobacteria by the lack of the 2-oxoglutarate synthase (EC 1.2.7.3) [33]. The implication of this is that PHAs are not an *a priori* energy storing compound in cyanobacteria, as acetyl-CoA can not be fully oxidized via the TCA cycle and, hence, no energy is produced from their catabolism [21]. A possible carbon storage function can not be ruled out, but the presence of the universal carbon storage compound glycogen undermines this option.

In order to gain new insights into the function of PHAs in cyanobacteria, we undertook a series of experiments to determine the effects of nutrient starvation and the resulting electron imbalances on PHA accumulation, the response of PHA biosynthesis to different carbon sources and the genetic regulation of the PHA synthase and other enzymes involved in acetate uptake in the model organism *Synechocystis* sp. PCC6803.

In a first series of experiments we determined the differential accumulation of PHAs under varying nitrate, phosphorus and combined nitrogen and phosphorus starvation conditions. The results shown in

figure 3 summarize our findings on the influence of nutrient starvation conditions and balanced,

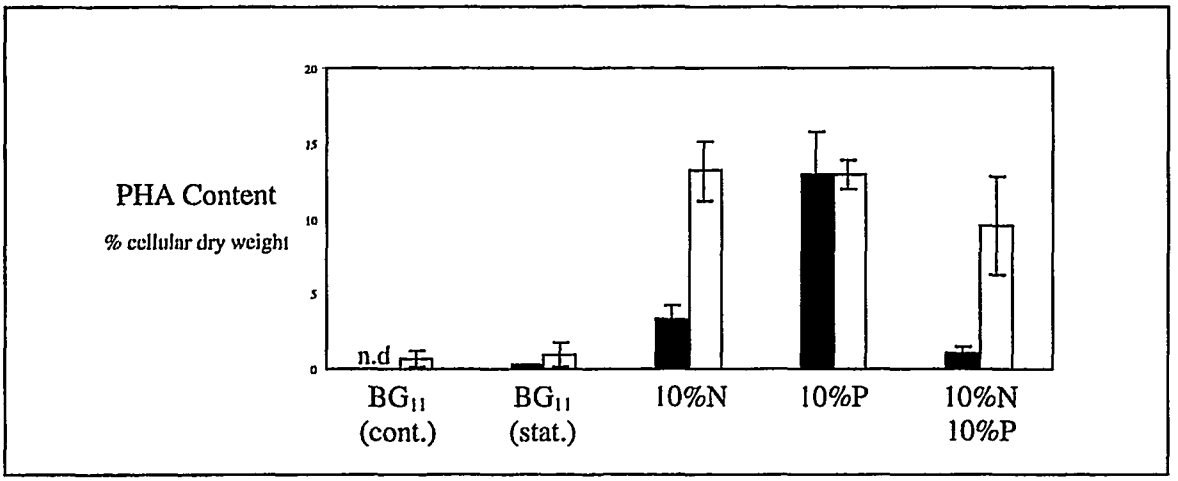

Figure 3. PHA content of *Synechocystis* sp. PCC6803 grown with different carbon sources and under different nutrient limitations in fed-batch or batch culture. The cells were harvested after 8 days of fed-batch culturing ($O.D._{730}$ approx. 0.8)(BG_{11}(cont.)) or four days in stationary growth phase (all other treatments). (Solid bars indicate no addition of acetate, open bars addition of 10mM acetate to the corresponding medium; labels on abscissa indicate the different nutrient limitation regimes: BG_{11} (control full medium); cont., continuous growth; stat., stationary growth phase; percentages refer to specific nutrient content in the growth medium relative to the base medium BG_{11} ($NaNO_3$, 17.65mM; K_2HPO_4, 0.18mM)(n.d., not detected; error bars show S.E. (n=2)).

continuous growth versus stationary phase conditions.

PHA accumulation is very low or not detectable under balanced, continuous growth conditions or when carbon becomes limiting at the onset of the stationary phase. The addition of acetate to the medium increases the biosynthesis of PHA, but the levels still do not exceed 1-2% of the cellular dry weight. In contrast, nitrogen starvation elicits a significant increase in PHA accumulation during the stationary phase. The presence of acetate clearly enhances the effect of nitrogen starvation. Nitrogen limitation induces a characteristic set of physiological responses in cyanobacteria that include cessation of cell division and degradation of the phycobilisomes, pigment-protein complexes that harvest most of the light energy for these organisms [34]. The increased accumulation of PHA observed here is most probably a result of the general imbalance of the carbon to nitrogen ratio in the cells resulting from an excess of carbon skeletons relative to the nitrogen available for amino acid biosynthesis.

Phosphate limitation has a more dramatic effect on PHA accumulation than nitrogen starvation. Regardless of the nature of the carbon source, inorganic only (CO_2) or in combination with an organic source (Na acetate), PHAs were accumulated to high levels. The highest concentration observed was close to 35% cellular dry weight under 6μM K_2HPO_4 (equivalent to 3% of the full medium; data not shown). Similarly to nitrogen starvation, phosphate starvation elicits a set of characteristic responses in the cells that include an increased synthesis of high affinity transport systems for phosphate and the production of hydrolytic enzymes, such as extracellular phosphatases, that allow utilization of alternate forms of phosphate. The effects of the combined nitrogen and phosphate starvation are most similar to those of nitrogen limitation only, because the overall effect of nitrogen starvation on the cell's metabolism is probably more significant than that of phosphate.

A second level of our investigation was to determine the actual regulation of the pha synthase in *Synechocystis* at the genetic and biochemical levels. The data summarized in table I show the effects of nitrate starvation and carbon source on the activity in crude extract of the pha synthase and the phosphotransacetylase. The levels of phosphotransacetylase are relevant because they reflect the level of acetyl-CoA, the direct precursor of PHA, in the cell. The results show a clear lack of response of the intracellular PHA synthase levels to acetate availability in the medium or acetyl-CoA levels in the cell. While the total transacetylase activity increased predictably with the addition of Na acetate to the medium, the expression levels of the PHA synthase remained constant. Conversely, nitrogen starvation clearly induced the levels of PHA synthase in the cell, while phosphotransacetylase activities remained constant across treatments.

Table I

PHA synthase and phosphotransacetylase activities in crude extracts of *Synechocystis* sp. PCC6803

Enzyme assayed and growth conditions[a]	Enzyme activity (± S.E.)[b] (nmol × min^{-1} × mg of $prot^{-1}$)	
	- Acetyl phosphate	+Acetyl phosphate
PHA synthase		
N_F	321.36 (± 8.23)	437 (± 32.03)
$N_{10\%}$	898.8 (± 42.6)	830.25 (± 37.3)
Phosphotransacetylase (EC 2.3.1.8)		
N_F	5762 (± 258.5)	13755 (± 632.9)
$N_{10\%}$	4783 (± 1758)	13006 (± 1838)

[a] Cells were harvested at the beginning of the stationary growth phase; cells were grown in full BG_{11} medium (N_F) or in BG_{11} medium containing only 10% of the original $NaNO_3$ (final N concentration 1.765 mM; $N_{10\%}$)

[b] The organic carbon source acetyl phosphate was added to the medium at a final concentration of 10 mM

Previous studies have shown that the control of PHA synthase is mediated by acetyl phosphate in *Synechococcus* sp. [35]. We conducted a series of analysis to determine the effect of acetyl phosphate on the activity of the *Synechocystis* sp. PHA synthase and obtained similar results indicating that this enzyme is regulated with substrate inhibition-like kinetics (data not shown). Phosphate concentration has also been shown before to regulate transcription of the PHA biosynthetic genes in *Acinetobacter* sp. isolated from activated sludge. In this instance, transcriptional activation of the pha_{Ac} gene cluster under phosphate starvation conditions is determined by the presence of an 18 bp consensus *pho* box in the promoter region typical of promoters in the *pho* regulon [36]. A detailed analysis of the promoter regions of the two pha_{Syn} PHA biosynthetic gene clusters reveals the absence of any *pho* box-like sequences but the near identity between the critical -35 and -10 σ^{70}-like motives between both clusters, which raises the possibility of parallel regulation and constitutive expression of the two pha_{Syn} gene clusters [24].

The overall regulatory scheme of PHA biosynthesis in *Synechocystis* sp. PCC6803 that is starting to emerge from this work is represented in figure 4. The direct effects of modulators such as acetyl

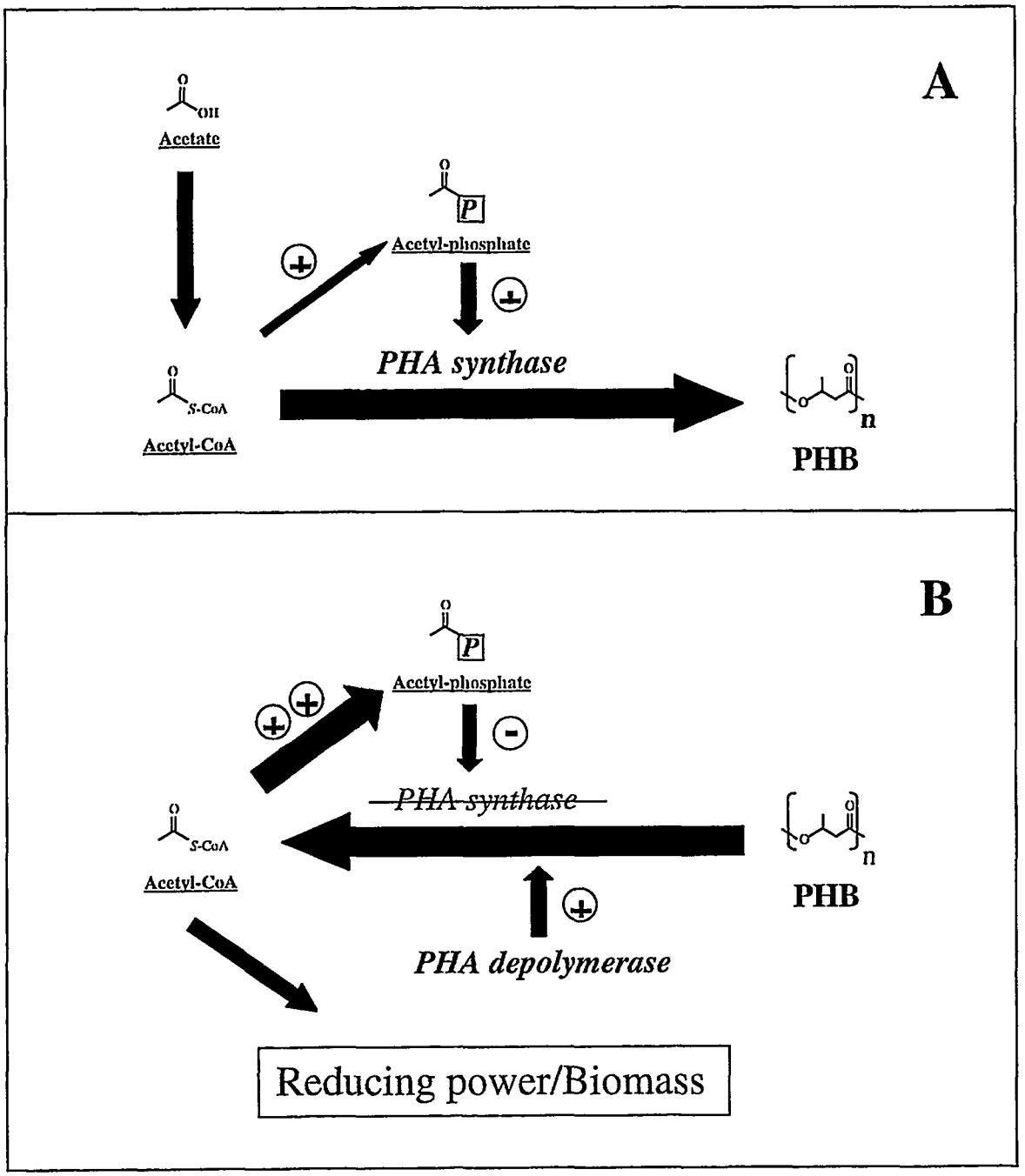

Figure 4. Conceptual representation of PHA synthase regulation by acetyl-phosphate in *Synechocystis* sp. PCC6803. (**A**) Activation of the PHA synthase at intracellular concentrations of acetyl phosphate below 3 mM. (**B**) Inactivation of the PHA synthase at intracellular concentrations of acetyl phosphate in excess of 3 mM resulting from the mobilization of PHAs for the production of biomass and an increase in the $NADPH_2/NADH_2$ pool available for cellular metabolism. ("+" and "-" signs denote activation and inhibition respectively)

phosphate, an indicator of acetyl-CoA concentrations in the cell, the substrate concentration effects as seen from the influence of acetate concentrations on PHA accumulation, and the global response mechanisms due to nutrient starvation conditions, show that the control of PHA biosynthesis in this organism is multi dimensional and occurring at the physiological as well as biochemical level. Ongoing research in our laboratory is addressing issues such as the influence of physiological imbalances in the intracellular reducing power pools on PHA accumulation patterns.

REFERENCES

(1) UNEP/WMO "United Nations Framework Convention on Climate Change," Climate Change Secretariat, 1992.
(2) Hoffert, M. I.; Caldeira, K.; Jain, A. K.; Haites, E. F.; Harvey, L. D. D.; Potter, S. D.; Schlesinger, M. E.; Schneider, S. H.; Watts, R. G.; Wigley, T. M. L.; Wuebbles, D. J. *Nature* **1998**, *395*.
(3) Steinbüchel, A. In *Novel biomaterials from biological sources*; Byrom, D., Ed.; MacMillan: New York, 1991.
(4) Doi, Y. *Microbial polyesters*; VCH Publishers, 1990.
(5) Poirier, Y.; Nawrath, C.; Somerville, C. *Biotechnology* **1995**, *13*, 142-50.
(6) Asada, Y.; Miyake, M.; Miyake, J.; Kurane, R.; Tokiwa, Y. *Int. J. Biol. Macromol.* **1999**, *25*, 37-42.
(7) Kurano, N.; Sasaki, T.; Miyachi, S. In *Advances in chemical conversions for mitigating carbon dioxide*; Inui, T., Anpo, M., Yanagida, S., Yamaguchi, T., Eds.; Elsevier Science:, 1998; Vol. 114.
(8) Moroney, J. V.; Somanchi, A. *Plant Physiol.* **1999**, *119*, 9-16.
(9) Ohtaguchi, K.; Kajiwara, S.; Mustaqim, D.; Takahashi, N. *Energy Conv. Mgmt.* **1997**, *38*, S523-S528.
(10) Hai, T.; Oppermann-Sanio, F. B.; Steinbüchel, A. *FEMS Microbiol. Lett.* **1999**, *181*, 229-36.
(11) Murakami, M.; Ikenouchi, M. *Energy Convers. Mgmt.* **1997**, *38*, S493-S497.
(12) Huntley, M. E.; Niiler, P. P.; Redalje, D. USA, 1996.
(13) Lagarde, D.; Beuf, L.; Vermaas, W. *Appl. Environ. Microbiol.* **2000**, *66*, 64-72.
(14) Thiel, T. In *The Molecular Biology of Cyanobacteria*; Bryant, D. A., Ed.; Kluwer Academic Publishers:, 1994.
(15) Williams, J. G. K. *Meth. Enzymol.* **1988**, *167*, 766-78.
(16) Taroncher-Oldenburg, G.; Stephanopoulos, G. Submitted.
(17) Peoples, O. P.; Sinskey, A. J. *J. Biol. Chem.* **1989**, *264*, 15298-303.
(18) Suzuki, T.; Miyake, M.; Tokiwa, Y.; Saegusa, H.; Saito, T.; Asada, Y. *Biotechnol. Lett.* **1996**, *18*, 1047-50.
(19) Miyasaka, H.; Nakano, H.; Akiyama, H.; Kanai, S.; Hirano, M. In *Advances in chemical conversions for mitigating carbon dioxide*; Inui, T., Anpo, M., Yanagida, S., Yamaguchi, T., Eds.; Elsevier Science:, 1998; Vol. 114.
(20) Carr, N. G. *Biochim. Biophys. Acta* **1966**, *120*, 308-10.
(21) Stal, L. J. *FEMS Microbiol. Rev.* **1992**, *103*, 169-80.
(22) Kaneko, T.; Sato, S.; Kotani, H.; Tanaka, A.; Asamizu, E.; Nakamura, Y.; Miyajima, N.; Hirosawa, M.; Sugiura, M.; Sasamoto, S.; Kimura, T.; Hosouchi, T.; Matsuno, A.; Muraki, A.; Nakazaki, N.; Naruo, K.; Okumura, S.; Shimpo, S.; Takeuchi, C.; Wada, T.; Watanabe, A.; Yamada, M.; Yasuda, M.; Tabata, S. *DNA Res.* **1996**, *3*, 109-36.
(23) Hein, S.; Tran, H.; Steinbüchel, A. *Arch. Microbiol.* **1998**, *170*, 162-170.
(24) Taroncher-Oldenburg, G.; Nishina, K.; Stephanopoulos, G. Submitted.
(25) Rehm, B. H. A.; Steinbüchel, A. *Int. J. Biol. Macromol.* **1999**, *25*, 3-19.
(26) Jia, Y.; Kappock, T. J.; Frick, T.; Sinskey, A. J.; Stubbe, J. *Biochem.* **2000**, *39*, 3927-36.
(27) Liebergesell, M.; Steinbüchel, A. *Eur. J. Biochem.* **1992**, *209*, 135-50.
(28) Liebergesell, M.; Steinbüchel, A. *Appl. Microbiol. Biotechnol.* **1992**, *38*, 493-501.
(29) Liebergesell, M.; Mayer, F.; Steinbüchel, A. *Appl. Microbiol. Biotechnol.* **1993**, *40*, 292-300.
(30) Van Gemerden, H. *Arch. Mikrobiol.* **1968**, *64*, 118-24.
(31) Satoh, H.; Mino, T.; Matsuo, T. *Int. J. Biol. Macromol.* **1999**, *25*, 105-9.
(32) Allen, M. M. *Ann. Rev. Microbiol.* **1984**, *38*, 1-25.
(33) Smith, J. *Ann. Microbiol. (Inst. Pasteur)* **1983**, *134 B*.
(34) Schwarz, R.; Grossman, A. R. *Pro. Natl. Acad. Sci. USA* **1998**, *95*, 11008-13.
(35) Miyake, M.; Kataoka, K.; Shiral, M.; Asada, Y. *J. Bacteriol.* **1997**, *179*, 5009-13.
(36) Schembri, M. A.; Bayly, R. C.; Davies, J. K. *J. Bacteriol.* **1995**, *177*, 4501-7.

Final List of Participants

18th Symposium on Energy Engineering Sciences

May 15-16, 2000

Argonne National Laboratory
Argonne, Illinois

Bassem Armaly
Division of Materials Sciences and Engineering, SC 131
U.S. Department of Energy
Office of Basic Energy Sciences
19901 Germantown Road
Germantown, MD 20874-1290
Phone: 301.903.4062
Fax: 301.903.0271
E-Mail: bassem.armaly@science.doe.gov

S. George Bankoff
Chemical Engineering Department
Northwestern University
Evanston, IL 60208
Phone: 847.491.5267
Fax: 847.491.3728
E-Mail: gbankoff@northwestern.edu

Jacob Barhen
Center for Engineering Science Advanced Research
Oak Ridge National Laboratory
P.O. Box 2008
1000 Bethel Valley Road
Oak Ridge, TN 37831-6355
Phone: 865.574.7131
Fax: 865.574.0405
E-Mail: barhenj@ornl.gov

Gabriel Bitton
Ctr. for Eng. Sci. Adv. Res./Computer Sci.& Mathematics
Oak Ridge National Laboratory
P.O. Box 2008
1000 Bethel Valley Road
Oak Ridge, TN 37831-6355
Phone: 865.241.2065
Fax: 865.574.0405
E-Mail: bittong@ornl.gov

John Blair
Council on Energy Engineering Research (CEER)
25 Moore Road
Wayland, MA 01778
Phone: 508.358.7568
Fax: 508.358.7568
E-Mail: jblair@world.std.com

Harvey W. Blanch
Department of Chemical Engineering
University of California-Berkeley
Tan Hall
Berkeley, CA 94720
Phone: 510.642.1387
Fax: 510.643.1228
E-Mail: blanch@socrates.berkeley.edu

Yehuda Y. Braiman
Ctr. for Eng. Sci. Adv. Res./Comp. Sci. & Mathematics
Oak Ridge National Laboratory
P.O. Box 2008
1000 Bethel Valley Road
Oak Ridge, TN 37831-6355
Phone: 865.241.2065
Fax: 865.574.0405
E-Mail: braimany@ornl.gov

Frederick W. Brust, Jr.
Department of Engineering Mechanics
Battelle Memorial Institute
505 King Avenue, Rm. 11-4-122
Columbus, OH 43201
Phone: 614.424.5034
Fax: 614.424.3457
E-Mail: brust@battelle.org

Raffi Budakian
Department of Physics
University of California-Los Angeles
Los Angeles, CA 90095
Phone:
Fax:
E-Mail: budak@physics.ucla.edu

Ivan Catton
Department of Mechanical and Aerospace Engineerin
University of California-Los Angeles
405 Hilgard Avenue
Los Angeles, CA 90095-1597
Phone: 310.825.5320
Fax: 310.206.4830
E-Mail: catton@ucla.edu

Yok Chen
Department of Materials Sciences
U.S. Department of Energy
19901 Germantown Road
Germantown, MD 20874-1290
Phone: 301.903.4174
Fax: 301.903.9513
E-Mail: yok.chen@science.doe.gov

Xinyu Fu
School of Nuclear Engineering
Purdue University
1290 Nuclear Engineering Building
West Lafayette, IN 47907
Phone: 765.494.5759
Fax: 765.494.9570
E-Mail: fu0@ecn.purdue.edu

Michael Cross
Department of Physics
California Institute of Technology
MS 114-36
Pasadena, CA 91125
Phone: 626.395.4320
Fax: 626.683.9060
E-Mail: mcc@caltech.edu

Henry S. Greenside
Department of Physics
Duke University
P.O. Box 90305
Durham, NC 27708-0305
Phone: 919.660.2548
Fax: 919.660.2525
E-Mail: hsg@phy.duke.edu

James R. Fincke
Department of Optical and Plasma Physics
INEEL
P.O. Box 1625
Idaho Falls, ID 83415-2211
Phone: 208.526.2031
Fax: 208.526.5327
E-Mail: jf1@inel.gov

Daniel D. Joseph
Department of Aerospace and Mechanics
University of Minnesota
110 Union Street, SE
Minneapolis, MN 55455
Phone: 612.625.0309
Fax: 612.626.1558
E-Mail: joseph@aem.umn.edu

Daniel Frederick
Department of Engineering Science and Mechanics
Virginia Polytechnic Institute and State University
MC 0219
Blacksburg, VA 24060
Phone: 540.231.3270
Fax: 540.231.6903
E-Mail: dfundfff@vt.edu

David L. Jung
CESAR, Computer Science and Mathematics Division
Oak Ridge National Laboratory
P.O. Box 2008
1000 Bethel Valley Road
Oak Ridge, TN 37831-6355
Phone: 865.241.2985
Fax: 865.241.0381
E-Mail: jungdl@ornl.gov

L. B. Freund
Division of Engineering
Brown University
182 Hope Street
Providence, RI 02912
Phone: 401.863.1476
Fax: 401.863.2857
E-Mail: freund@engin.brown.edu

Seungjin Kim
School of Nuclear Engineering
Purdue University
Hangar No. 3, Purdue Airport
West Lafayette, IN 47906
Phone: 765.494.5759
Fax: 765.494.9570
E-Mail: seungjin@ecn.purdue.edu

Gunol Kojasoy
Department of Mechanical Engineering
University of Wisconsin-Milwaukee
P.O. Box 784
Milwaukee, WI 53201
Phone: 414.229.5639
Fax: 414.229.6958
E-Mail: kojasoy@uwm.edu

Francis C. Moon
Department of Mechanical and Aerospace Engineeri
Cornell University
204 Upson Hall
Ithaca, NY 14853-7501
Phone: 607.255.7146
Fax: 607.255.1222
E-Mail: fcm3@cornell.edu

Katja Lindenberg
Department of Chemistry and Biochemistry 0340
University of California-San Diego
9500 Gilman Drive
La Jolla, CA 92093-0340
Phone: 858.534.3285
Fax: 858.534.7244
E-Mail: klindenberg@ucsd.edu

Chris D. Muzny
National Institute of Standards and Technology
MS 838.07
325 Broadway
Boulder, CO 80303
Phone: 303.497.5549
Fax: 303.497.5224
E-Mail: chris.muzny@nist.gov

Uwe Lommatzsch
Department of Chemistry
Stanford University
Mudd Building, MC 5080
Stanford, CA 94305-5080
Phone: 650.723.4332
Fax: 650.725.0259
E-Mail: lommatz@stanford.edu

N. Sri Namachchivaya
Department of Aero & Astro Engineering
University of Illinois
306 Talbot Laboratory
Urbana, IL 61801
Phone: 217.244.0683
Fax: 217.244.0720
E-Mail: sri@nsgsun.aae.uiuc.edu

Arun Majumdar
Department of Mechanical Engineering
University of California-Berkeley
6185 Etcheverry Hall
Berkeley, CA 94720
Phone: 510.643.8199
Fax: 510.642.6163
E-Mail: majumder@me.berkeley.edu

Joseph J. O'Gallagher
Department of Physics
The University of Chicago
Enrico Fermi Institute
5640 South Ellis Avenue
Chicago, IL 60637
Phone: 773.702.7757
Fax: 773.702.6317
E-Mail: j-ogallagher@uchicago.edu

Mark J. McCready
Department of Chemical Engineering
University of Notre Dame
182 Fitzpatrick Hall
Notre Dame, IN 46556
Phone: 219.631.7146
Fax: 219.631.8366
E-Mail: mjm@nd.edu

Alfonso Ortega
Dept. of Aerospace and Mechanical Engineering
The University of Arizona
P.O. Box 210119
1130 North Mountain
Tucson, AZ 85721
Phone: 520.621.6787
Fax: 520.621.8191
E-Mail: ortega@u.arizona.edu

Lynne E. Parker
Center for Engineering Science Advanced Research
Oak Ridge National Laboratory
P.O. Box 2008
1000 Bethel Valley Road
Oak Ridge, TN 37831-6355
Phone: 865.241.4959
Fax: 865.574.0405
E-Mail: parkerle@ornl.gov

Seth J. Putterman
Department of Physics
University of California-Los Angeles
Los Angeles, CA 90095
Phone: 310.825.2269
Fax: 310.206.5668
E-Mail: puherman@ritva.physics.ucla.edu

Tomio Y. Petrosky
Center for Statistical Mechanics and Complex Systems
The University of Texas-Austin
RLM 7.220
Austin, TX 78712
Phone: 512.471.7253
Fax: 512.471.9621
E-Mail: petrosky@physics.utexas.edu

Nageswara S.V. Rao
Computer Science and Mathematics Division
Oak Ridge National Laboratory
P.O. Box 2008
1000 Bethel Valley Road
Oak Ridge, TN 37831-6355
Phone: 865.574.7517
Fax: 865.241.0381
E-Mail: raons@ornl.gov

Robert Price
Division of Materials Sciences and Engineering, SC 131
U.S. Department of Energy
Office of Basic Energy Sciences
19901 Germantown Road
Germantown, MD 20874-1290
Phone: 301.903.3565
Fax: 301.903.0271
E-Mail: bob.price@science.doe.gov

Walter G. Reuter
Materials Department
INEEL
P.O. Box 1625
Idaho Falls, ID 83415-2218
Phone: 208.526.1708
Fax: 208.526.0690
E-Mail: wgr2@inel.gov

Vladimir A. Protopopescu
Computer Science and Mathematics Division
Oak Ridge National Laboratory
P.O. Box 2008
1000 Bethel Valley Road
Oak Ridge, TN 37831-6355
Phone: 865.574.4722
Fax: 865.574.0405
E-Mail: vvp@ornl.gov

Hermann Riecke
Department of Applied Mathematics
Northwestern University
2145 Sheridan Road
Evanston, IL 60208
Phone: 847.491.3345
Fax: 847.491.2178
E-Mail: h-riecke@nwu.edu

David Y. H. Pui
Department of Mechanical Engineering
University of Minnesota
111 Church Street, SE
Minneapolis, MN 55455
Phone: 612.625.2537
Fax: 612.625.6069
E-Mail: dyhpui@tc.umn.edu

Herschel B. Smartt
Industrial and Material Technologies Department
INEEL
P.O. Box 1625
Idaho Falls, ID 83415-2210
Phone: 208.526.8333
Fax: 208.526.0690
E-Mail: hbs@inel.gov

Todd R. Smith
School of Nuclear Engineering
Purdue University
West Lafayette, IN 47907
Phone: 765.494.5759
Fax: 765.494.9570
E-Mail: trsmith@helios.ecn.purdue.edu

Charles R. Tolle
Industrial and Material Technology Department
INEEL
P.O. Box 1625
Idaho Falls, ID 83415-2210
Phone: 208.526.1895
Fax: 208.526.0690
E-Mail: tollcr@inel.gov

Pol D. Spanos
Dept. of Civil & Mechanical Engineering
Rice University
MS-321, P.O. Box 1892
Houston, TX 77251
Phone: 713.348.4909
Fax: 713.348.5191
E-Mail: spanos@rice.edu

Jack C. Wells
Computer Science and Engineering Division
Oak Ridge National Laboratory
P.O. Box 2008
1000 Bethel Valley Road
Oak Ridge, TN 37831
Phone: 865.241.2853
Fax: 865.241.0381
E-Mail: wellsjc@ornl.gov

Gregory Stephanopoulos
Department of Chemical Engineering
Massachusetts Institute of Technology
Building 56, Rm. 469
77 Massachusetts Avenue
Cambridge, MA 02139
Phone: 617.253.4583
Fax: 617.253.3122
E-Mail: gregstep@mit.edu

Roland Winston
Department of Physics
The University of Chicago
Enrico Fermi Institute
5640 South Ellis Avenue
Chicago, IL 60637
Phone: 773.702.7756
Fax: 773.702.6317
E-Mail: winston@rainbow.uchicago.edu

Xiaodong Sun
School of Nuclear Engineering
Purdue University
1290 Nuclear Engineering Building
West Lafayette, IN 47906
Phone: 765.494.5759
Fax: 765.494.9570
E-Mail: xsun@ecn.purdue.edu

Lei Zhang
Ctr. for Eng. Science & Advanced Research Ctr.
Oak Ridge National Laboratory
P.O. Box 2008, 6010, MS 6355
1000 Bethel Valley Road
Oak Ridge, TN 37831-6355
Phone: 865.241.2061
Fax: 865.241.0381
E-Mail: zhang@ornl.gov

Yupin Sun
Department of Physics
The University of Chicago
Enrico Fermi Institute
5640 South Ellis Avenue
Chicago, IL 60637
Phone: 773.702.7759
Fax: 773.702.6317
E-Mail: yupinsun@midway.uchicago.edu